International Journal of Greenhouse Gas Control 145 (2025) 104388

Contents lists available at ScienceDirect

International Journal of Greenhouse Gas Control

journal homepage: www.elsevier.com/locate/ijggc

Flow2Quake, an integrated multiphase flow, geomechanical and seismicity model for efficient forecasting of injection and extraction induced earthquakes

Mateo Acosta [a,d,*,1], Thomas Ledevin [a,c,1], Guillaume Salha [a,c], Charles Forestier [a,c], Lucie Michelin [b,c], Xiaojing Fu [b], Jean-Philippe Avouac [a,b]

[a] Geological and Planetary Sciences, California Institute of Technology, Pasadena, CA, USA
[b] Mechanical and Civil Engineering, California Institute of Technology, Pasadena, CA, USA
[c] École Polytechnique, Institut Polytechnique de Paris, Palaiseau, France
[d] Now at Department of Geosciences Virginia Tech, Blacksburg, VA, USA

ARTICLE INFO

Dataset link: 10.17605/OSF.IO/WSH32

Keywords:
Reduced order model
Carbon capture and storage
Multiphase vertical flow equilibrium
Gas injection/extraction
Geomechanical modeling
Induced seismicity
Decatur
Groningen

ABSTRACT

Efforts to secure and decarbonize the energy sector are driving various subsurface reservoir operations. These operations carry a risk of inducing surface deformation and earthquakes. To assess these risks, modeling tools integrating fluid flow, geomechanical and seismicity modeling are needed. Here, we demonstrate the use of an efficient Vertical Flow Equilibrium (VFE) multiphase fluid flow model in an integrated framework for deformation and seismicity modeling both under fluid extraction or injection configurations. The VFE-computed spatio-temporal pressure evolution is fed to a geomechanical module to compute surface deformation and stress changes in and around the reservoir. Stress changes feed a seismicity module to calculate earthquake probabilities. First, we apply the benchmarked model to gas extraction from Groningen. There, we can reduce the variance of pressure measurements by ~38% with respect to a pre-existing single phase flow model while remaining computationally efficient. The surface deformation and seismicity simulations show remarkable agreement with observed data. Second, we study induced seismicity due to CO_2 sequestration in the Decatur phase 1 project. We find that, for the Decatur phase 1 project, poroelastic stress changes can account for most of the non-clustered observed seismicity within modeling uncertainties. Finally we simulate scenarios for CO_2 sequestration using the Quest field. The sloping reservoir topography significantly impacts the predicted position of the CO_2 plume but the effects on geomechanical deformation (and seismicity) are minimal. Incorporating VFE models with geomechanical and seismicity forecasts with real-world case applications can allow real-time hazard assessment and mitigation procedures.

1. Introduction

Subsurface operations involving fluid injection/extraction such as carbon capture and storage (Celia et al., 2015; Kelemen et al., 2019), hydrogen extraction (Zgonnik, 2020) and storage (Zivar et al., 2021), hydrocarbon extraction, wastewater injection, and geothermal energy can help address some of the world's most pressing challenges in climate mitigation, energy security, and water scarcity (Stephenson et al., 2019). However, these subsurface operations also carry the risk of fluid leakage to aquifers or to the surface (Gholami et al., 2021), of surface deformation, and of fluid-induced seismicity (Rutqvist, 2011; Grigoli et al., 2017; Keranen and Weingarten, 2018). These risks can jeopardize the safety and economic value of these operations. In that regard, models that can be used to assess the safe design and guide operations in real-world scenarios are crucial for the long-term deployment of these technologies.

The geohazards mentioned above arise due to the interactions between fluids and the rock formation. At its minimal complexity, one-way coupled models evaluate the pore pressure change due to subsurface operations and the resulting geomechanical deformation, ignoring the feedback on the reservoir porosity and permeability (Bachu et al., 2007; Kopp et al., 2009). More sophisticated models account for the two-way coupling between fluid flow and geomechanical deformation based on the macroscopic theory of poroelasticity (Detournay and Cheng, 1993; Wang and Kümpel, 2003; Hao et al., 2012; Jha and

* Correspondence to: 926 W Campus Dr, Blacksburg, VA 24060, USA.
E-mail address: acosta@vt.edu (M. Acosta).
[1] Equal contributions.

https://doi.org/10.1016/j.ijggc.2025.104388
Received 5 September 2024; Received in revised form 16 April 2025; Accepted 21 April 2025
Available online 28 May 2025

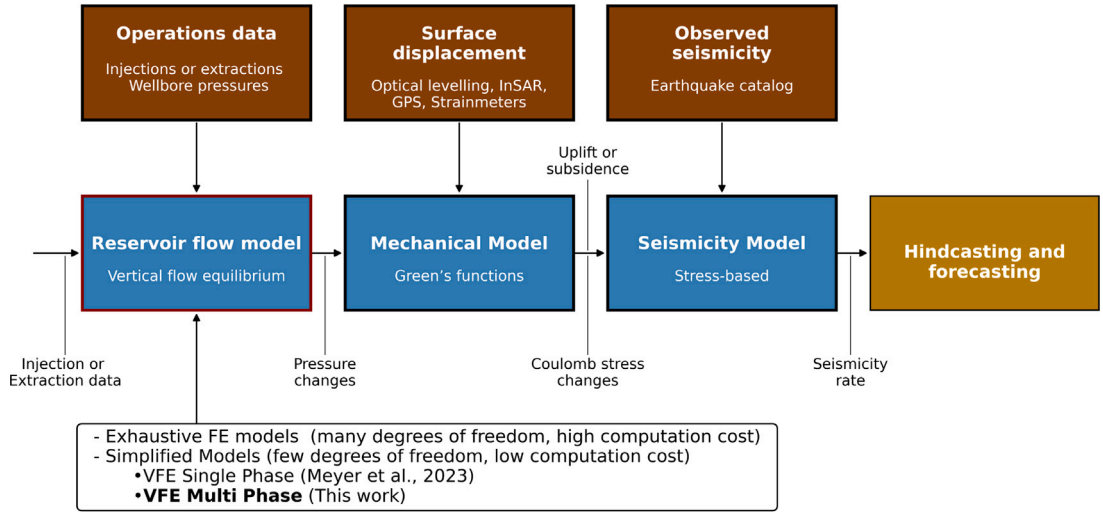

Fig. 1. Integrated modeling workflow for deformation and seismicity forecasting, FLOW2QUAKE (modified from Acosta et al. (2023)). The workflow allows modular simulation of fluid pressure due to reservoir operations (injection or extraction), the resulting geomechanical deformation, and eventual induced seismicity. The blue boxes represent the different modules, that are calibrated using observational data (red boxes). The current article focuses on the development of our data-ready module for multiphase flow modeling of fluid injections or extractions in/from subsurface porous reservoirs.

Juanes, 2014) or on more general models of poromechanics (Bemer et al., 2001; Coussy, 2004; Bjørnarå et al., 2016). At the maximum complexity, three-dimensional models are developed to fully couple multiphase fluid flow with geomechanical processes, which allows embedding faults in the 3D domain to investigate mechanistic details for diagnosis (Juanes et al., 2016; Buijze et al., 2017; Im and Avouac, 2021). These fully coupled reservoir, geomechanical and seismicity models capture the important multiphysics processes at play. However, they are computationally costly, and therefore inadequate for probabilistic analysis, uncertainty quantification and real-time data assimilation. Various strategies have therefore been explored to reduce the computational cost of such simulations:

1. Use analytical solutions for the fluid flow and geomechanical deformation coupling (Rudnicki, 1986; Detournay and Cheng, 1993), and relate the stress changes to seismicity rate changes with a seismicity model (Segall and Lu, 2015; Bourne et al., 2018; Zhai et al., 2019; Li et al., 2021; Kim and Avouac, 2023). This solution can be extremely efficient computationally but cannot incorporate spatial variations of reservoir transport or geomechanical properties. Moreover, the range of physical processes that can be included is limited. It does not apply to multiphase flow or thermo-hydraulic flow for example.
2. Vertically integrate the coupled equations for fluid flow and geomechanical deformation (Bjørnarå et al., 2016) and solve numerically for the coupled fields, or alternatively, precompute the response functions of the coupled equations (Andersen et al., 2017). Potentially integrate geomechanical deformation with a seismicity model (this has not been done to the best of our knowledge).
3. Sequentially couple the fluid flow and geomechanical models (Dempsey and Suckale, 2017; Bourne et al., 2018; Candela et al., 2019; Richter et al., 2020; Smith et al., 2022; Meyer et al., 2022; Acosta et al., 2023). This method applies for reservoirs where the geomechanical deformation has a small effect on changes in reservoir's porosity and permeability. It has the major advantage that each simulation module (reservoir fluid flow, geomechanical deformation, seismicity model) can be run independently to account for the needed complexity.

The last approach is for example adopted in the development of FLOW2QUAKE, a modular integrated workflow for reservoir flow, geomechanical and seismicity modeling (Meyer et al., 2022; Acosta et al., 2023) (Fig. 1). This workflow has been successfully tested in the case of the Groningen gas field where gas production has resulted in significant and well-documented deformation and seismicity. The computational efficiency has allowed considering short timescale pressure and stress variations over long overall operation times, thus providing improved knowledge of the deformation and seismicity generation processes (Acosta et al., 2023; Tamama et al., 2024). It also allowed quantifying the uncertainty associated with the seismicity forecast using Bayesian statistics (Kaveh et al., 2023). This highlights the benefits of efficient numerical modeling workflows for fluid flow, geomechanical deformation and induced seismicity forecasting. In these aforementioned works, a single phase reservoir flow model that approximates the gas/brine system as a single phase mixture was adopted (Meyer et al., 2022). However, the lack of two-phase flow physics leads to increases of the errors between the modeled and measured pressures over time (Meyer et al., 2022). Such inconsistency can hinder the applicability of the modeling workflow to cases where multiphase flow effects could be more significant. Moreover, in the case of a CO_2 injection, a single phase flow model does not calculate the spatial footprint of the CO_2 plume, which is key to evaluate potential leakage through faults or legacy wells (Celia et al., 2015).

A major challenge with using the state-of-the-art reservoir multiphase flow models in operation-driven seismicity prediction framework is their computational cost, which depends on (i) the dimensions of the problem, (ii) the number and the mathematical structure of the equations (e.g., linearity, time dependency and coupling). The balance between numerical expense and accuracy is at the heart of reservoir modeling and various approaches have been taken to tackle this issue. A particularly efficient approach is the Vertical Flow Equilibrium (VFE) model, as it reduces one spatial dimension in the reservoir flow model (Cardoso et al., 2009; Gasda, 2010; Nordbotten and Celia, 2012; Guo et al., 2014; Court et al., 2012; Bjørnarå et al., 2016; Cowton et al., 2018; Bandilla et al., 2019; Jenkins et al., 2019; Meyer et al., 2022). This intermediate complexity approach can be applied in reservoirs whose lateral dimensions are much larger than their vertical thickness. Reviews on the applicability of such approach to multiphase flow physics (Court et al., 2012; Bandilla et al., 2019) have shown that this type of simplified model can often be applied to gas extraction or injection into brine-filled reservoirs (Fig. 3). To this end, multiphase VFE models (MP-VFE) can be used to evaluate pressure dynamics during geologic carbon sequestration (Gasda, 2010; Court et al., 2012; Szulczewski et al., 2012; Nordbotten and Celia, 2012; Celia et al., 2015;

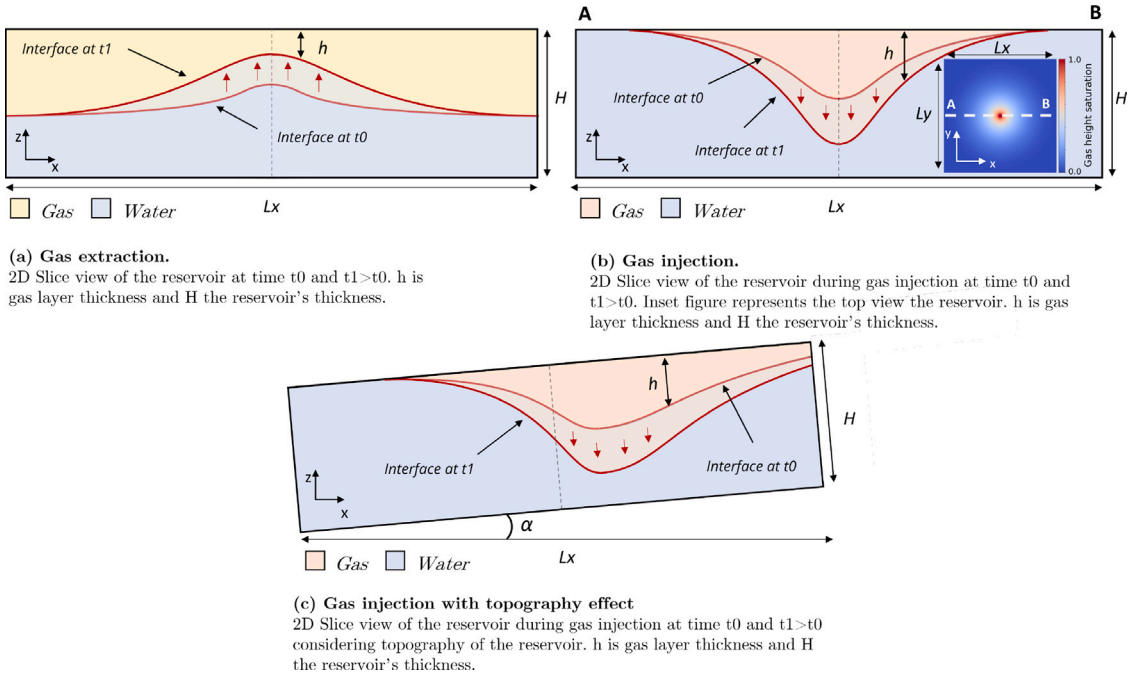

(a) Gas extraction.
2D Slice view of the reservoir at time t0 and t1>t0. h is gas layer thickness and H the reservoir's thickness.

(b) Gas injection.
2D Slice view of the reservoir during gas injection at time t0 and t1>t0. Inset figure represents the top view the reservoir. h is gas layer thickness and H the reservoir's thickness.

(c) Gas injection with topography effect
2D Slice view of the reservoir during gas injection at time t0 and t1>t0 considering topography of the reservoir. h is gas layer thickness and H the reservoir's thickness.

Fig. 2. Vertical cross sections of an idealized subsurface porous reservoir with a central well (dashed line) used for gas extraction (a) or injection (b,c). The gas (red/orange) is assumed less dense than the brine. The shape of the gas plume results from the interplay between natural convection and pressure dynamics of the reservoir. In (a) and (b) the top of the reservoir is assumed perfectly horizontal while in (c) a slope is considered resulting in a component of gravity driven flow.

Bjørnarå et al., 2016; Bandilla et al., 2019; Jenkins et al., 2019; Zhao et al., 2024).

In this work, we use a MP-VFE model to feed pressure changes to geomechanical deformation and seismicity models and test its performance in real reservoir operations. This reservoir modeling framework is selected for the following reasons: (1) it is vertically integrated, which reduces the problem dimension and enables faster computation; (2) it has the capability to consider spatially variable reservoir properties such as permeability, porosity, thickness and topography (variations in vertical depth) as well as the effect of gas buoyancy. It integrates seamlessly into the modular workflow for geomechanical deformation and seismicity forecasting and thus allows probabilistic analysis of the forecasts and real-time optimization procedures.

Hereafter, we first briefly describe the multiphase reservoir flow model, its numerical solution, and the integration of the reservoir flow model with geomechanics and seismicity modeling (Section 2). We then apply and discuss our model for two practical cases (1) gas extraction from the Groningen gas field and associated seismicity (Section 3); (2) CO_2 injection in the Decatur phase 1 pilot project (Section 4) . Finally, we explore fluid-flow related implications of our model on deformation and seismicity using scenarios for the Quest CCS field where data is not available yet to fully calibrate the models (Goertz-Allmann et al., 2024) (Section 5).

2. Methods

2.1. The VFE model for gas and pressure dynamics

2.1.1. Model assumptions and description

The vertical flow equilibrium approach, detailed in Yortsos (1995), Gasda (2010) and Nordbotten and Celia (2012), reformulates the classic subsurface flow equations based on the assumption of hydrostatic (or non hydrostatic Nordbotten and Celia, 2006) fluid pressure in the vertical direction. Thus, the resulting model does not need to account for *nonequilibrium* dynamics of pressure in the vertical dimension, reducing the problem dimension by one (i.e., the z direction). For a two-dimensional problem (i.e., in the x-y plane) main assumptions (Gasda, 2010; Nordbotten and Celia, 2012; Court et al., 2012; Celia et al., 2015; Bandilla et al., 2019) for the two-phase VFE model are :

1. The timescale to achieve pressure equilibrium along the vertical dimension τ_z is much shorter than that along the horizontal dimension τ_x. Such assumption (Yortsos, 1995), can be applied if:

$$R_L = \sqrt{\frac{\tau_x}{\tau_z}} = \frac{L_x}{L_z}\sqrt{\frac{k_z}{k_x}} \gg 10, \tag{1}$$

where k_x and k_z are the lateral and vertical permeability of the rock, L_x and L_z are the lateral and vertical characteristic lengths. Here, the diffusive timescale is defined as $\tau_d = L_d^2/D_d$. D_d is the diffusion coefficient along direction $d \in \{x, z\}$, calculated as $D_d = k_d/(\phi c \mu)$, where μ and c are the viscosity and fluid compressibility, respectively. This assumption is valid in many high-porosity, high-permeability underground reservoirs whose lateral extent is much larger than their thickness, and the permeability shows limited anisotropy in the horizontal and vertical dimensions (Fig. 3). For example, in the case of the Groningen reservoir in the northeastern Netherlands, $R_L > 117$, in the Decatur CCS projects in the Illinois Basin, USA, $R_L > 60$, and in the Quest CCS reservoir in central Alberta, CA, $R_L > 500$.
2. The sharp interface assumption is valid in cases where the strong buoyant drive from the density difference between gas and brine (see Fig. 2). Because we focus here on pressure changes at the reservoir scale (a few tens of kilometers), and at timescales of several decades, we neglect the timescale for fluid segregation, allowing the use of a sharp interface separating the two fluid phases (Court et al., 2012).

For illustrating the model, a subsurface reservoir whose geometry is a rectangular prism with fixed thickness H, fixed length L_x and fixed width L_y (equal here) is considered (Fig. 2). This geometry allows presenting the model equations but the numerical implementation allows changes of H in the horizontal plane. The reservoir rock has porosity

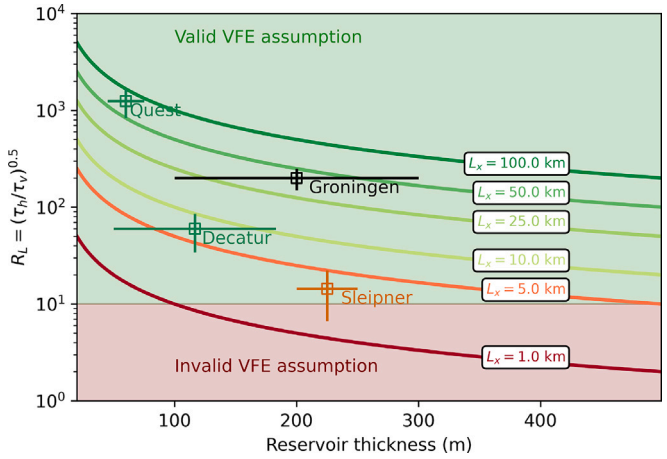

Fig. 3. Validity of the VFE assumption. Ratio of timescales for horizontal to vertical fluid diffusion (Eq: (1)) versus reservoir thickness for isotropic permeabilities. Colored lines correspond to fixed horizontal length scales found in conventional reservoirs. The gas extraction and injection reservoirs from this study are reported. We add the Sleipner reservoir for reference.

$\phi(x, y)$, permeability $k(x, y)$ and is filled with two immiscible fluids separated by a sharp interface representing the capillary transition zone. An initially homogeneous residual dissolved gas concentration C_g inside the water region (blue zone in Fig. 2) is imposed. Mass transfer between fluids is not considered in this work for simplicity but the model could be expanded to account for CO_2 dissolution effects (Guo et al., 2014). Fig. 2 shows vertical cross-sections of an idealized reservoir with a well located in the middle is used for injection (Fig. 2b, c) or extraction (Fig. 2a).

For the case of a perfectly horizontal reservoir top (Fig. 2a–b), the evolution of each phase can be described using mass conservation and Darcy's law:

$$Gas: \begin{cases} \frac{\partial}{\partial t}\left(\rho_g \phi C_g\right) + \nabla.\left(\rho_g \boldsymbol{q_g}\right) = I_g, \\ \boldsymbol{q_g} = \frac{-k k_{rg}}{\mu_g} \nabla p_g, \end{cases} \tag{2}$$

$$Water: \begin{cases} \frac{\partial}{\partial t}\left(\rho_w \phi C_w\right) + \nabla.\left(\rho_w \boldsymbol{q_w}\right) = I_w, \\ \boldsymbol{q_w} = \frac{-k k_{rw}}{\mu_w} \nabla p_w, \end{cases} \tag{3}$$

where C_g and C_w represent the dissolved gas and water concentrations and ρ_g and ρ_w are the gas and water densities, which can be found from fluid equations of state (Bell et al., 2014) and interpolated for computational efficiency (see Appendix A1) if the pressure and temperature range during the reservoir lifetime can be estimated to the first order. I_g and I_w are the source terms and g is the gravitational acceleration. Finally, k_{rd} represents the relative permeability of d phase.

Integration of equations Eqs. (2) and (3) yields a coupled h (the thickness of the gas layer in space) and p^i (the pressure at the gas/water interface in space). Assuming that the vertical flow is negligible compared to lateral flow, and assuming that densities and viscosities vary near-linearly with pressure (single phase; Appendix A1) the system of equations becomes (Gasda, 2010; Nordbotten and Celia, 2012; Jenkins et al., 2019):

$$\begin{aligned} &(1-C_g)\rho_g \phi \left(\left(c_r + c_g \frac{\rho_g^0}{\hat{\rho_g}} \right) \left(h + \frac{C_g}{(1-C_g)} H \right) \frac{\partial p^i}{\partial t} + \frac{\partial h}{\partial t} \right) \\ &- \nabla.\left(\rho_g \lambda_g h \left(\nabla p^i - \rho_g g \nabla h \right) \right) \\ &= H I_g, \end{aligned} \tag{4}$$

$$\begin{aligned} &(1-C_g)\rho_w \phi \left(\left(c_r + c_w \frac{\rho_w^0}{\rho_w} \right) (H-h) \frac{\partial p^i}{\partial t} - \frac{\partial h}{\partial t} \right) \\ &- \nabla.\left(\rho_w \lambda_w (H-h) \left(\nabla p^i - \rho_w g \nabla h \right) \right) \\ &= H I_w, \end{aligned} \tag{5}$$

where $\lambda_g = \frac{k k_{rg}}{\mu_g}$ and $\lambda_w = \frac{k k_{rw}}{\mu_w}$ are the fluid mobilities, c_r, c_w, and c_g are the rock, water, and gas compressibilities respectively. Here ρ_g^0 is the gas density at the initial pressure before operations, and $\hat{\rho_g}$ is the vertical averaged density of gas in the plume (see Appendix A for details). Note that these equations allow heterogeneity in reservoir thickness H in the lateral direction (e.g., $H(x, y)$).

Reservoir topography may have an important impact on the gas plume dynamics due to buoyancy effects of gas-water flow (Gasda, 2010; Cowton et al., 2018; Afanasyev et al., 2022). To consider a spatially variable reservoir topography, i.e. variations in the depth of reservoir's top and/or bottom that leads to sloping (Gasda, 2010), the necessary modifications are shown in Eqs. (B10) and (B11) in Appendix.

2.1.2. Numerical implementation

We use the FEniCS finite element software (Logg et al., 2012), to which we input the *weak formulation* of Eqs. (4) and (5):

$$\begin{aligned} &\int_\Omega (1-C_g)\phi \left(\left(c_r + c_g \frac{\rho_g^0}{\rho_g} \right) \left(h + \frac{C_g}{(1-C_g)} H \right) \frac{\partial p^i}{\partial t} + \frac{\partial h}{\partial t} \right) v_1 \mathrm{d}v \\ &+ \int_\Omega \lambda_g h \left(\nabla p^i - \rho_g g \nabla h \right) . \nabla v_1 \mathrm{d}v \\ &= \int_\Omega \frac{H I_g}{\rho_g} v_1 \mathrm{d}v, \\ &\int_\Omega (1-C_g)\phi \left(\left(c_r + c_w \frac{\rho_w^0}{\rho_w} \right) (H-h) \frac{\partial p^i}{\partial t} - \frac{\partial h}{\partial t} \right) v_2 \mathrm{d}v \\ &+ \int_\Omega \lambda_w (H-h) \left(\nabla p^i - \rho_w g \nabla h \right) . \nabla v_2 \mathrm{d}v \\ &= \int_\Omega \frac{H I_w}{\rho_w} v_2 \mathrm{d}v, \end{aligned} \tag{6}$$

where v_1 and v_2 are test functions, and Ω is the test function space. We use a solver based on Newton's method with incremental convergence criteria, and an auto-adaptive time stepping method to maximize the stability of the model (Logg et al., 2012). We use continuous, piecewise quadratic Lagrange finite elements on a triangular mesh.

We approximate the point source term (at coordinates (x_s, y_s)) as a Dirac function with a narrow Gaussian distribution (here for the gas phase but it can be similarly written for water):

$$I_g = \frac{\dot{M}_g}{H} \frac{1}{\pi \sigma^2} e^{\frac{-(x-x_s)^2-(y-y_s)^2}{\sigma^2}}, \tag{7}$$

where the standard deviation σ is chosen such that, far from the well, the diffusion process is not impacted by the shape of the source. Typically, the characteristic length of the gas diffusion $\mathcal{L} = \sqrt{D_h T}$ (where T is the total duration of injection/extraction) needs to respect $\mathcal{L} \gg \sigma$.

We use local mesh refinement in order to resolve the dynamics near injection/extraction wells while keeping an overall coarse numerical mesh to reduce computational cost. In particular, (1) in the immediate vicinity of the wells we impose small elements ($\mathrm{d}x_1 \ll \sigma$); (2) close to the wells we impose medium elements ($\sigma < \mathrm{d}x_2 \ll \mathcal{L}$); (3) far away from the wells, we impose large elements ($\mathcal{L} < \mathrm{d}x_3$). As an example of the computational mesh, we show the one used for Groningen in Fig. 7D (inset). The choice of the mesh refinement affects injected pressure and volume results but the code is flexible enough that it allows the user to select the amount of local mesh refinement. A convergence study needs to be run for different case scenarios, depending on the injection/extraction rates, time discretization and

mesh refinement. For the cases studied here (Benchmarks, Groningen, Decatur phase 1, and the Quest scenario), we systematically verified that the solution gradually converged toward a stable value, and that mass conservation between the target extraction/injection mass and the actual numerically computed mass was respected.

2.2. Integration with geomechanical deformation and seismicity models

Fluid injections/extractions in/from the subsurface can induce surface deformation and seismicity. Therefore, reservoir fluid flow modeling is the initial step for forecasting subsidence and seismicity. In this section, we detail how the multiphase VFE model described in Section 2.1.1 is integrated with an efficient geomechanical model used to calculate deformation and stress in and around a reservoir, and a stress-based seismicity forecasting model as shown in Fig. 1.

2.2.1. Geomechanical deformation

We use the poroelastic geomechanical model of Smith et al. (2022) to relate the fluid pressure changes to stress changes within and outside the reservoir. The computed field of fluid pressure changes from the reservoir flow model (ΔP) is combined with the reservoir's uniaxial compressibility field (C_m) such that the reservoir compaction writes:

$$C = C_m(x,y).\Delta p(x,y,t).H(x,y) \tag{8}$$

The reservoir is discretized into cuboidal volumes geometrically defined by $L_x.L_y.H(x,y)$ that deform poroelastically and represent first order variations in reservoir geometry. The relation between poroelastic compaction and displacement ($U(x,y,z)$) or stress ($\sigma(x,y,z)$) uses a semi analytical Green's function approach combined with a strain-volume formulation (Geertsma, 1973; Kuvshinov, 2008) that takes the form:

$$U(x,y,z) = -\Delta p.C_m.F_{U(x,y,z)}(vertices, observation\ points) \tag{9}$$

$$\sigma(x,y,z) = -\Delta p.C_m.F_{\sigma(x,y,z)}(vertices, observation\ points) \tag{10}$$

with F_U, and F_σ functions of the cuboid's position (vertices), and the observation points (where displacements or stresses need to be sampled), and $\Delta p.C_m = \epsilon_{el}$ the elastic strain from reservoir compaction. For details on the functions, the reader is referred to Geertsma (1973), Kuvshinov (2008), Li et al. (2021) and Smith et al. (2022). From the changes in shear stress ($\Delta\tau(x,y,z,t)$) and effective normal stress ($\Delta\sigma'_N(x,y,z,t) = \Delta\sigma_N(x,y,z,t) - \Delta p(x,y,z,t)$), the changes in Coulomb stress are:

$$CFS(x,y,z,t) = \Delta\tau(x,y,z,t) - f.\Delta\sigma'_N(x,y,z,t) \tag{11}$$

with $f \sim 0.6$ the static friction coefficient of the reservoir rock. Note that we adopt the convention that the normal stress is positive in compression.

Detailed advantages and validations of this model are provided in Smith et al. (2022) and Meyer et al. (2022). The geomechanical model builds on Geertsma (1973) and Kuvshinov (2008)'s works which deal with a poroelastic nucleus and volume of strain respectively embedded in an elastic half-space. Smith et al. (2019, 2022) demonstrated that the poroelastic deformation produced by representing the reservoir as a grid of polyhedral volumes of strain is comparable to analytical solutions for the thin sheet poroelastic model of Bourne and Oates (2017). Such approach effectively serves as a benchmark of the vertically integrated pressure model and geomechanical coupling. It is valid for thin reservoirs where the porosity/permeability changes with deformation are negligible toward the initial values.

The Green's Functions relating reservoir compaction to displacements and stress changes outside the reservoir need to be calculated once (Kuvshinov, 2008) in a similar approach to Andersen et al. (2017). Then, through the dot product of the Green's functions (F_U, and F_σ) and the reservoir's strain ($\epsilon(x,y,z,t)$) at each time step, we can recover the spatio-temporal evolution of displacements and stresses outside of the reservoir. This approach makes the model computationally efficient and reproduces well stress changes in a 3D volume (Smith et al., 2022). In our workflow (Fig. 1), the outcome of this module is then used to feed the seismicity model.

2.2.2. Seismicity model

We relate the changes in Coulomb stress (CFS, Eq: (11)) to seismicity rate changes (R) using a given 'failure function' which can take several functional forms (Bourne et al., 2018; Dempsey and Suckale, 2017; Smith et al., 2022; Heimisson et al., 2022; Dieterich, 1994; Zhai et al., 2019; Dahm and Hainzl, 2022). Here, we adopt the Threshold Rate and State function which relates the response of a potentially seismic source to stress changes, accounts for time lag related to the characteristic time of earthquake nucleation using Rate and State friction (RS) (Dieterich, 1994), and allows the population of faults being far from criticality (Heimisson et al., 2022). Heimisson et al. (2022) showed that the seismic productivity in response to stress changes of sources that follow Rate and State failure laws can the be expressed as:

$$\frac{R}{r} = \begin{cases} \frac{exp(\frac{CFS(t)-CFS_c}{a\sigma_0})}{1+\frac{1}{t_a}\int_{t_b}^{t} exp(\frac{CFS(t')-CFS_c}{a\sigma_0})dt'} & \text{if } t \geq t_b \\ 0 & \text{if } t < t_b \end{cases} \tag{12}$$

with $t_a = \frac{a\sigma_0}{\dot{\tau}}$ the characteristic time of the earthquake nucleation process under secular loading rate ($\dot{\tau}$), $a\sigma_0$ the friction-stress parameter of the RS failure law, and r the background seismicity rate. In this formulation there is no assumption regarding the criticality of the sources and the critical stress threshold CFS_c has to be passed to produce seismicity at time t_b (Dieterich, 1994; Heimisson et al., 2022). The choice of this failure function accounts for the necessity of a time-dependence in the response of seismicity to stress changes (Acosta et al., 2023), and for a strength excess in induced seismicity settings (Heimisson et al., 2022; Acosta et al., 2023). The procedure for uncertainty quantification from this modeling workflow is detailed by Kaveh et al. (2023).

2.3. Probabilistic seismicity causal attribution

Our modeling workflow accounts for seismicity driven by poroelastic stress transfers outside of the reservoir, and in addition pore fluid pressure diffusion inside the reservoir. However, as of now, FLOW2QUAKE does not account for other potential sources of seismicity like tectonic loading, inter-earthquake triggering, aseismic slip triggering, or fluid diffusion along pre-defined faults (Brodsky and Lajoie, 2013; Wang et al., 2022; Wang and Avouac, 2025).

To apply FLOW2QUAKE to induced seismicity settings, we need to compare the modeled seismicity with seismicity whose cause can be related directly to the injection operations (Luu et al., 2022). To that end, we use the probabilistic causal inference method developed by Wang and Avouac (2025). The method is an extension of the declustering algorithm of Marsan and Lengline (2008). It uses non-parametric mean-field kernels whose amplitudes scale linearly with different triggers (seismic moment of earthquakes, hydraulic energy of injection for example). Linear intensity estimation of the kernels allows establishing a probabilistic causal structure of different triggers.

Regarding the applications in this work: (1) We neglect clustered seismicity in the Groningen case (Section 3) due to low earthquake clustering (7 to 28% clustered seismicity (Candela et al., 2019; Muntendam-Bos, 2020; Post et al., 2021; Trampert et al., 2022; Sirorattanakul et al., 2024). (2) The application to the Decatur phase 1 project (Wang and Avouac, 2025) showed that ~11% of the earthquakes there could be attributed to the injection itself while the rest could be attributed to other triggers. We will apply our method to the seismicity attributed to the fluid injection from here on (see Section 4). (3) No available information on seismicity can be accessed at the time of this publication for the Quest site so we focus on fluid flow and geomechanical deformation there in a scenario-based approach (Goertz-Allmann et al. (2024), see Section 5).

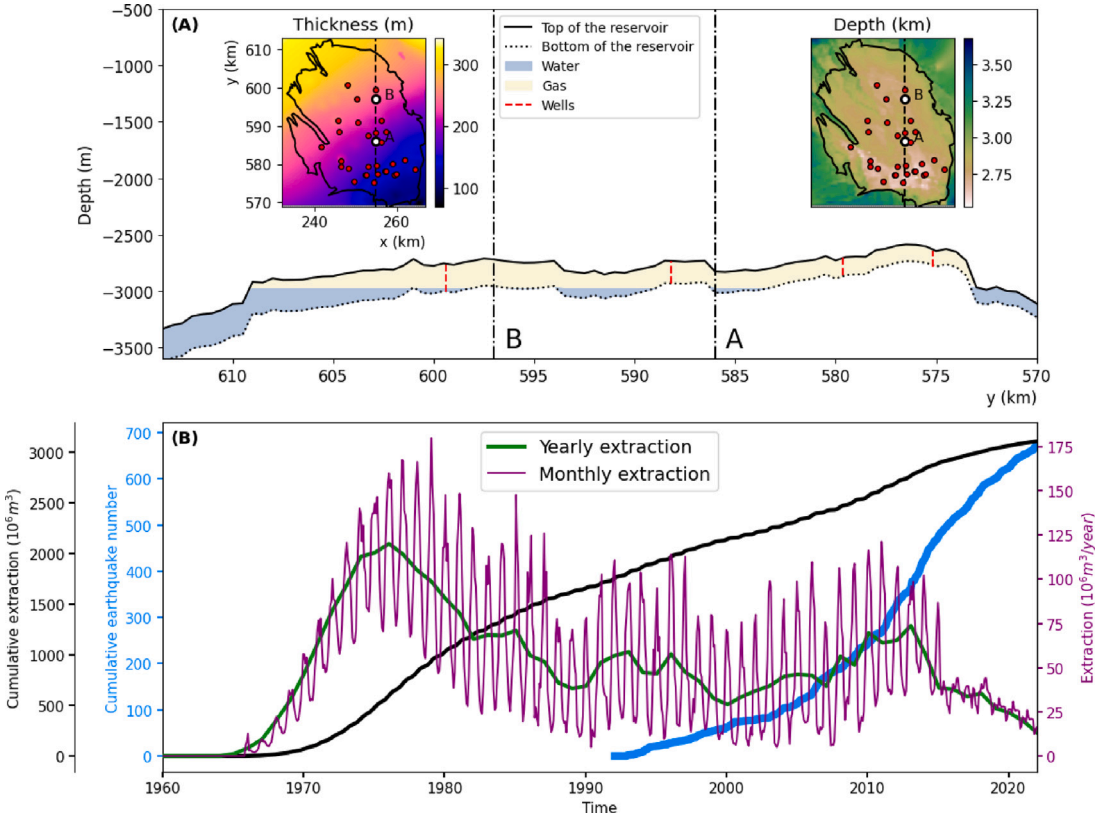

Fig. 4. The Groningen Gas reservoir. (a) Cross-section of the reservoir. Thick lines represent the Rotliegend formation's top and bottom along the dashed line shown in the insets. Insets show the depth and thickness of the reservoir from a top view. (b) Extraction and seismicity history around the gas field.
Source: Modified from Acosta et al. (2023).

3. Application to gas extraction from the Groningen gas field

3.1. The Groningen gas field

The Groningen field is Western Europe's largest gas reservoir, located in northeastern Netherlands. Gas is extracted from the Rotliegend sandstone formation at a depth of 3000 ± 500 m since 1963 (Burkitov et al., 2015). The reservoir extends laterally around 35 km by 50 km Burkitov et al. (2015), de Jager and Visser (2017) and Oates et al. (2022), and the formation's thickness varies between 70 m and 320 m inside the boundaries of the field (Fig. 4a, left inset). Gas extraction started in 1963 and a total of 29 well extraction clusters (dark blue area in Fig. 4a right-inset) extracted gas from the field. As of 2021, approximately 3000 out of ~4500 million m^3 of gas had been extracted and resulted in a pressure depletion of up to ~25 MPa.

Recent studies (Acosta et al., 2023; Kaveh et al., 2023; Tamama et al., 2024) have shown the benefit of using *monthly* time discretization for the calibration and uncertainty quantification of seismicity forecasting models. This highlights the need for computationally efficient reservoir and geomechanical models that resolve short temporal scales, as opposed to the yearly sampling used in previous studies (van Oeveren et al., 2017; Dempsey and Suckale, 2017; Bourne et al., 2018; Candela et al., 2019; Richter et al., 2020). The extraction configuration from 29 well clusters with monthly variations in production complicates the reservoir modeling compared to the example of a single well problem in our benchmark study, as the model needs to resolve complex well-well interactions. We simulate the Groningen gas field behavior using the real reservoir geometry and extraction data (Oates et al., 2022) shown in Fig. 4b).

3.2. Pressure diffusion model & history matching

We initialize our model based on the pressure measurements in the early days of gas extraction (from 1962 to 1965; Fig. 7, Burkitov et al. (2015)), which shows a uniform pressure of around 35 MPa. Initial dissolved gas and water concentration are chosen as constant and homogeneous. Above the gas-water interface, historical measurements show a zero water concentration, which guarantees a gas relative permeability of 1. Below the interface, the relative permeability of water is low and here considered as $k_{rw} = 0.071$ (Burkitov et al., 2015), in support of the assumption of a sharp interface. We apply no-flow Neumann boundary conditions on all boundaries of the reservoir for simplicity, although the simulator can also accommodate mixed boundary conditions in portions of the reservoir (Logg et al., 2012). More complex conditions would be needed to simulate fluid exchanges with aquifers adjacent to the field (van Oeveren et al., 2017) but this is left for future work. Three main unknown model parameters must be estimated: the initial amount of gas (i.e. the height of the gas column compared to the thickness of the reservoir at all (x, y) coordinates at time $t = 0$, the value being spatially homogeneous), the permeability (k), and the porosity (ϕ) of the rock formation. These parameters are determined by minimizing the difference between the simulated pressure fields and the pressure measurements. Porosity ϕ and permeability k are assumed spatially homogeneous and stationary in time for simplicity and computational efficiency. For the VFE model applied to Groningen, we will not consider the reservoir topography for simplicity (therefore using Eqs. (4) & (5) rather than Eqs. B10 & B11). Therefore, the equilibrium state is a field in which the gas column height is proportional to the reservoir thickness, and $h/H(t = t_0)$

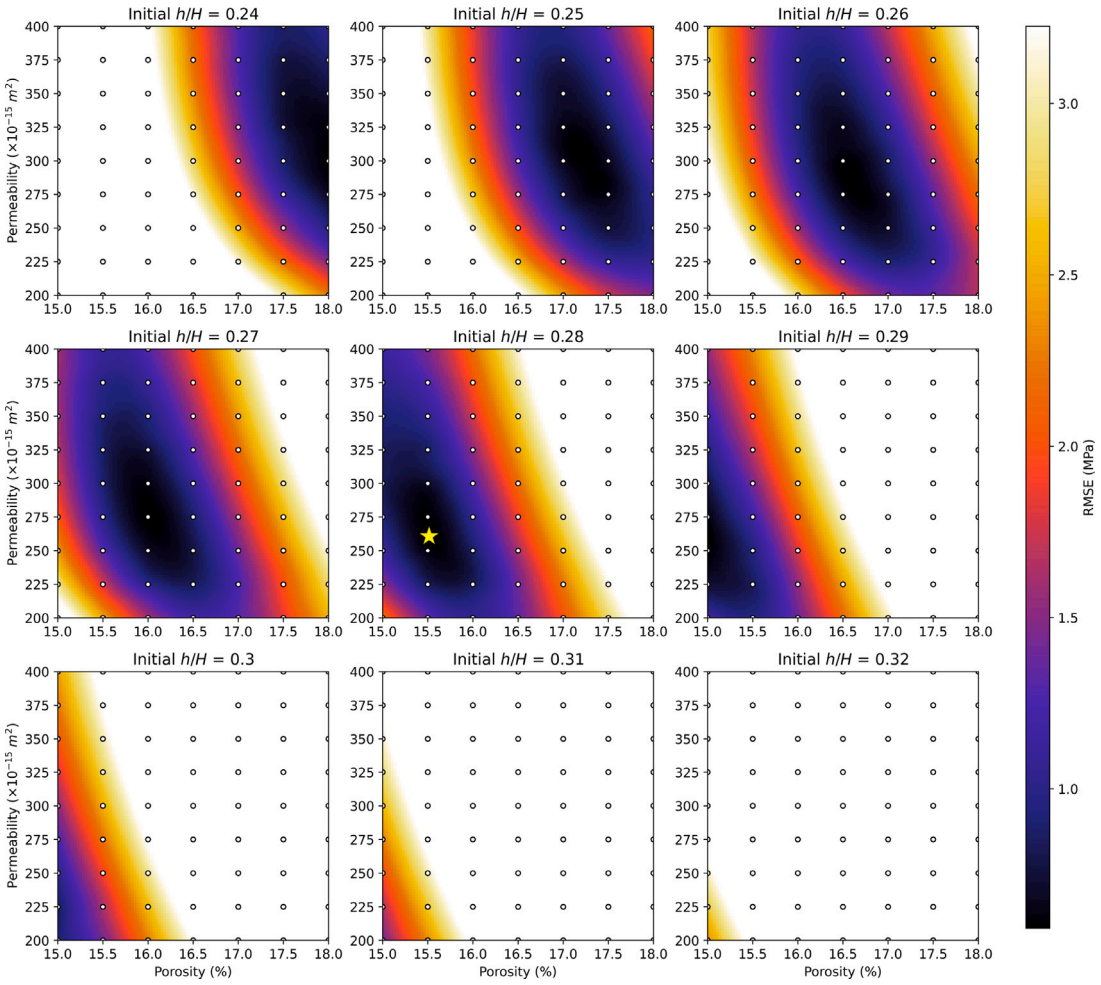

Fig. 5. Results of the MP-VFE history matching procedure. Permeability versus porosity for varying initial heights of the gas column. Colorbar shows the Root Mean Square Error calculated from comparing our model predictions with the pressure measurements. Yellow star shows the chosen best-fitting model for the rest of the simulations shown in this section.

represents the initial gas column height ratio, a parameter inverted for in the history matching procedure.

To determine the best set of parameters, we performed a history matching using 567 pressure measurements between 1963 and 2021. We use a grid search, scanning the following ranges of parameters: $\phi \in (0.15, 0.18)$, $k \in (200, 400) \times 10^{-15}$ m^2, and ratio $h(t = t_0)/H \in (0.24, 0.32)$. The results of history matching parameter space are presented in Fig. 5. For each value of the initial gas column height ratio, a minimum root mean square error (RMSE) can be found which is similar among the explored parameter space. To determine the best-fitting model parameters, we use a 3D interpolation in the space of initial gas column height ratio vs. RMSE, and then discriminate by comparing our permeability and porosity values to the reported values for Groningen (Burkitov et al., 2015): $\langle\phi\rangle = 17\%$ and $\langle k\rangle = 260 \times 10^{-15}$ m^2. We minimize the distance $d = \frac{\langle\phi\rangle - \phi}{\langle\phi\rangle} + \frac{\langle k\rangle - k}{\langle k\rangle}$ and obtain $\phi = 15.5\%, k = 264 \times 10^{-15}$ m^2, for an initial gas column height ratio of 0.28. The corresponding RMSE stands at 0.593 MPa. We note that the RMSE from the operator's model (MORES model, van Oeveren et al. (2017)) is of 0.548 MPa for 96 free parameters, while the RMSE from our former single phase flow model (Meyer et al., 2022) is of 0.956 MPa for 3 free parameters. By adding the multiphase physics to the problem we reduce the variance of the reservoir model by ∼38% considering only 3 free parameters. The computation time of each multiphase VFE model for the whole Groningen time–history using monthly discretization is of ∼7 min on the hardware described in Appendix C without any code optimization. This computational demand can be compared to ∼1 min for the single phase VFE model. The operator's model cannot be compared in terms of numerical computation as it is run on a high performance computing cluster of unknown specifications (van Oeveren et al., 2017).

Once the model is calibrated through the history matching procedure, we proceed to use the best parameters to generate the pore pressure diffusion in the reservoir during gas extraction operations and integrate the results with geomechanical and seismicity modeling.

3.3. Gas layer and pressure dynamics

One benefit of the multiphase VFE model compared to single phase model is that it computes the thickness of the gas layer within the reservoir as well as pressure. Fig. 6 shows the distribution of gas column height ratio from 1972 to 2020 and highlights the capabilities of the model to tackle interactions between wells. In the almost 50 years time span, it decreased to less than 24% (around 4% decrease) at some wells locations. Although remaining gas measurements in the Groningen reservoir indicate less than one third of the initial amount, gas saturation does not decrease by that amount due to fluid decompression as the overall reservoir pressure drops (Appendix A1). However, the mass of gas has decreased to less than two thirds of the initial mass present in the reservoir. It is noteworthy that some areas in the reservoir show a slight increase in gas column height ratio over time. This is due to the interactions between the boundaries of the reservoir and the extracting wells which can generate an overall shape of the interface that adapts to the extractions and boundaries in areas where wells do not operate.

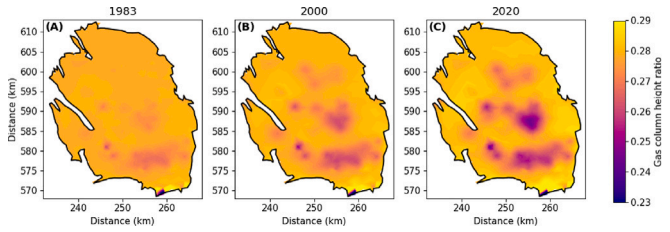

Fig. 6. Predicted gas column height ratio in the Groningen gas field at different times. Darker areas correspond to areas where the gas column has diminished most.

Fig. 7 shows the spatio temporal evolution of fluid pressure in the field. Temporal evolution of pressure at each well cluster (Fig. 7d) shows excellent agreement between our model (dashed lines) and observations (points) confirming a correct history match. There is a strong gradient in the reservoir fluid pressure from northwest to southeast in the early years of operations (Fig. 7a). Over the years, the pressure gradient decreases due to continued extraction (Fig. 7b,c). The pressure drop between 1960 and 2020 is of approximately 25 MPa on average throughout the reservoir.

3.4. Geomechanical and seismicity modeling

The fluid pressure changes generated by our history-matched model is the input into the geomechanical and seismicity modeling modules described in Section 2.2.

The spatiotemporal evolution of modeled surface subsidence, maximum Coulomb stress changes (hereafter denoted CFS to simplify notations), and seismicity are shown in Fig. 8. Regarding predicted surface deformation, we observe the development of a subsidence bowl in the center of the reservoir with increasing extraction as was observed in geodetic data for Groningen. Different areas in the reservoir present various amounts of subsidence over time consistently with the geodetic observations (Fig. 8a,d, to compare with Smith et al. (2019)). The maximum predicted surface subsidence between 1960 and 2021 is approximately 40 cm. The maximum Coulomb stress changes are not completely aligned in space with the areas of maximum surface subsidence because the presence of faults and their throws generate increases in CFS (Smith et al., 2022; Kaveh et al., 2023), as shown by comparing Fig. 8d and e. We observe a significant increase in CFS in the central-northern and south-western areas of the reservoir reaching up to 50 kPa computed 10 m above the reservoir. For details on how the spatial stress sampling affects the magnitude of CFS the reader is referred to Smith et al. (2022) and Kaveh et al. (2023). Finally, the seismicity density shows a spatial pattern similar to the distribution of maximum Coulomb stress changes. We observe a great match in the temporal and spatial structure of the seismicity (Fig. 8c, f) albeit a slight model over prediction in the southwestern area (compare to the inset of Fig. 8f).

3.5. Model comparison

We now compare the results of our geomechanical predictions when the fluid pressure is generated using (i) the operator's MORES model (Burkitov et al., 2015; van Oeveren et al., 2017; Oates et al., 2022), (ii) the single phase model (SP-VFE) of Meyer et al. (2022), and (iii) the multiphase model presented in this study (MP-VFE). To compare spatial variations, we first take the total changes in simulated fluid pressure, surface deformation, maximum Coulomb stress changes, at the timing of peak seismicity (by Jan-2014), and subtract them one-to-one. The comparison is presented in Fig. 9. Because the pressure measurements were collected more frequently during the first 20 years of production (1970–1990), the best-fitting pressure model obtained from history matching tend to match better the data from this period than the more recent data. This is an indication that our model might be missing factors of temporal variations of the pressure field. As we compare our model to surface deformation and seismicity observations mostly collected after 1990, the set of parameters $(k, \phi, \frac{h(t=0)}{H})$ are chosen so that the pressure at the end of the extraction is as close as possible to more recent pressure measurements (after 1990). The set of parameters chosen for the following is: $\phi = 16.2\%, k = 270e{-}15$ m^2, $\frac{h(t=0)}{H} = 27.8\%$ for a corresponding RMSE of 0.72 MPa. It is not the most optimal model to fit all the pressure data but is still a significant improvement with respect to the single phase flow model.

Regarding pressures, we observe that the differences between the MORES model and both the SP-VFE & MP-VFE are within ±2 MPa in the whole gas field (Fig. 9a). The largest differences between models occur in the south-western section of the reservoir because the MORES model introduces a permeability barrier along this area, which we have not accounted for in the SP or MP-VFE models to avoid fine-tuning. We observe that the difference between the SP-VFE and MP-VFE is within ≈1 MPa. We note that it is remarkable that the MP-VFE model, reduces the differences toward the MORES model in most of the field compared to the SP-VFE (Fig. 9a). It is likely that our model is not completely adequate in the south-west part of the field where, due to a reservoir structural high, the gas reservoir might not be connected to the main area (Fig. 4). In fact, de Jager and Visser (2017) and van Oeveren et al. (2017) inferred that a permeability barrier can be present and extends from center-west toward the south-east of the reservoir and can lead to a separated compartment in the south-west section of the reservoir. The residuals are a bit higher there than over the rest of the main part of the reservoir but small enough that the assumption of uniform properties seems acceptable. Note that the model could be adjusted better by accounting for the reservoir topography and allowing for spatial heterogeneity of its properties. The model would then approach further the performance of MORES but would lose the benefit of its simplicity and of the low computational cost of its calibration.

Regarding geomechanical deformation, we show the differences between model predictions in terms of surface subsidence (using the uniaxial compressibility derived with the MORES model and geodetic data by Smith et al. (2019)) and the resulting maximum Coulomb Stress changes in Fig. 9b and c, respectively. We observe that the geomechanical deformation is most severely underestimated when using the SP-VFE model, whose differences with respect to the MORES model go up to ~20–30 mm. The MP-VFE model improves the subsidence prediction except in the southwestern area (Fig. 9b). In terms of maximum CFS, both MP-VFE and SP-VFE result in a large difference in the predicted maximum CFS over the southwest area of the reservoir compared to the MORES model. The SP-VFE model also shows a large overestimation of stress in the central reservoir area (Fig. 9c), which is reduced by using the MP-VFE model.

Finally, regarding the seismicity forecasts, we show the results of our MCMC inversion in Fig. 10. In terms of the spatial density of seismicity (Fig. 10a, b, c), we observe that using the SP-VFE model, we predict ~10% more seismicity in the central and south-western parts of the reservoir but around 10% less seismicity outside the region when compared to the MP-VFE model (Fig. 10a). The MP-VFE model predicts a seismicity pattern which fits better the observed spatial distribution compared to SP-VFE model, and is closer to the seismicity predicted with MORES by about 10% globally (Fig. 10b, c.).

In terms of the temporal evolution of seismicity rates (Fig. 10d), the three models perform similarly from 1985–2013. Later, from 2013 to 2018, the MORES derived seismicity rates (and the associated epistemic uncertainties) are higher than the MP-VFE and SP-VFE derived ones. The latter two perform similarly with a slight undershoot by the MP-VFE derived model in the later period. We note that by the end of our hindcast (2023), the three models predict very similar seismicity rates. The different predicted stress changes are compensated by the adjustment of the seismicity model parameters (Fig. 10e–h). Note that the aleatoric uncertainty, which explains the variation of the observed

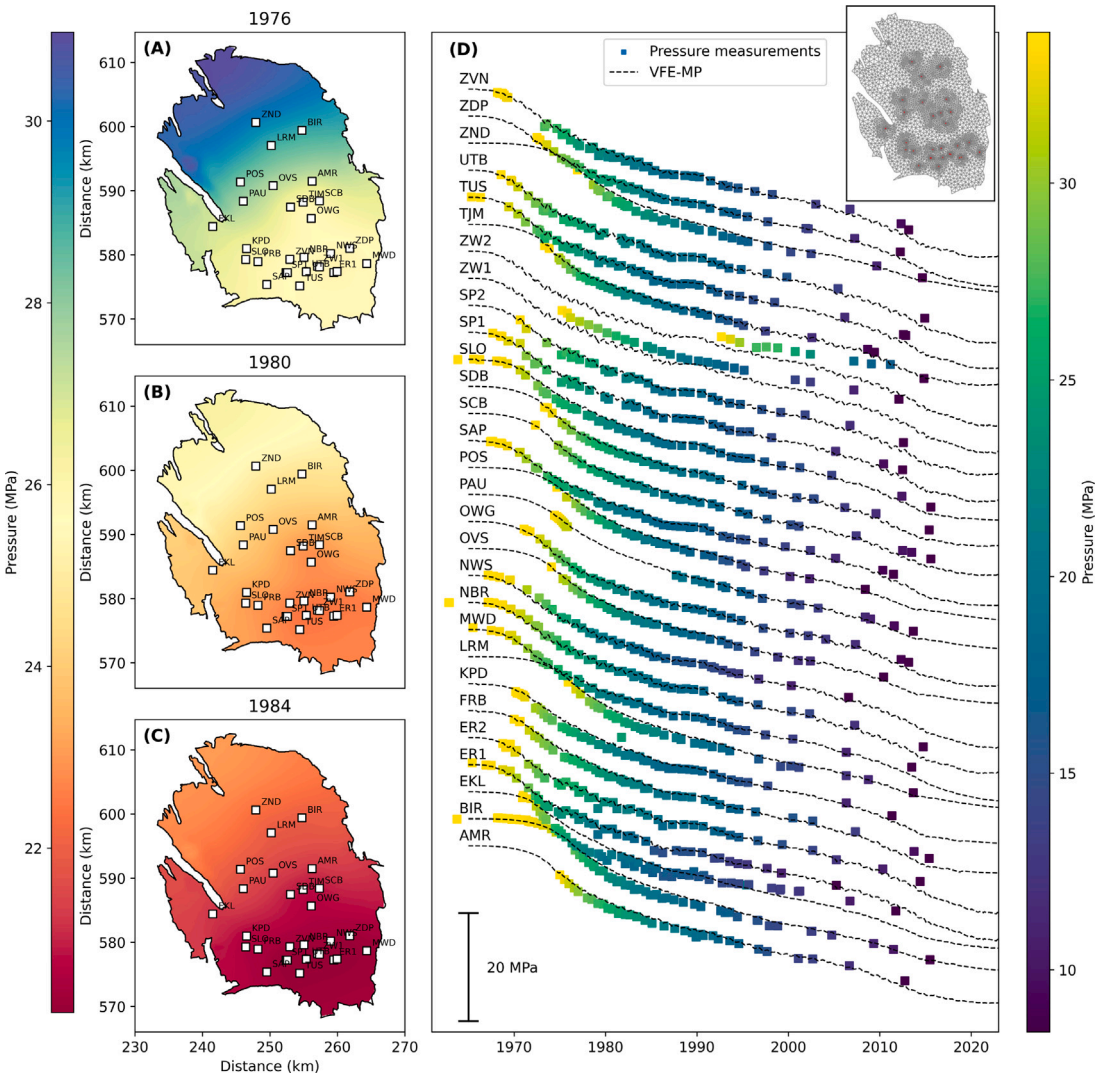

Fig. 7. Spatio temporal pressure evolution in Groningen predicted from our multiphase VFE model. (a,b,c) Top-views of the reservoir pressure the labeled times respectively. (d) Temporal evolution of fluid pressure at well clusters. Dashed lines show the model's predictions, and the points show the pressure measurements (Oates et al., 2022), showing the accuracy of the history matching procedure. Inset in panel d. shows the computational mesh used for this model.

seismicity beyond the epistemic uncertainty range (Kaveh et al., 2023), is not shown to avoid cluttering the figure.

These results highlight the benefits and usefulness of simpler or more complex models for the problem of estimating geomechanical deformation and potential induced seismicity. In the case of gas extraction from the Groningen gas field, we observe that accounting for the multiphase nature of the fluid-diffusion problem can significantly increase the accuracy on the pressure predictions (Fig. 9a) but has a smaller effect on the surface deformation (Fig. 9b), and spatial density of seismicity (Fig. 10a, b, c).

As such, it is important to keep in mind the objective when using simplified reservoir models in the integration of fluid diffusion, geomechanical deformation and seismicity modeling. If the objective is to predict the temporal evolution of seismicity rates, it would be sufficient to use a single phase flow model as shown in Fig. 10d. On the other hand, if one wants to accurately predict the surface subsidence/uplift associated with operations, it would be important to re-calibrate the geodetically-derived compressibility field for the pressure model in place (Li et al., 2024). Finally, if one wants to predict the pressures very accurately, or predict the spatio temporal evolution of the gas/brine interface, it would be necessary to account for the multiphase nature of the problem for example. We highlight that for CO_2 injection problems, it is important to estimate the spatial extent of the gas plume as described in the following section.

4. Application to carbon capture and storage in the Decatur phase 1 project

4.1. The Decatur phase 1 project

The Decatur IBDP phase 1 project is the first pilot project for CO_2 injection in the USA. It is hosted in the Illinois basin near the city of Decatur (Fig. 11). The CCS1 well injected captured CO_2 in the lower Mt. Simon formation (Fig. 11b) formed of high permeability sandstones (Greenberg, 2021). The lower Mt. Simon formation is thought to be hydraulically isolated from the rest of the 500 m thick Mt. Simon formation by interlacing mudstone layers near the location of CCS1 (Williams-Stroud, 2022; Silva et al., 2024)

About one million metric tonnes of CO_2 were injected at CCS1 from October 2011 to September 2014, at the CCS1 well (Greenberg, 2021; Williams-Stroud, 2022). The average injection rate was ~40 tonnes per hour (11 kg/s), with slight daily variations (Fig. 12). The initial reservoir pressure is of about 20 MPa. Reported monthly pressure variations at CCS1 wellhead (Greenberg, 2021; Williams-Stroud, 2022)

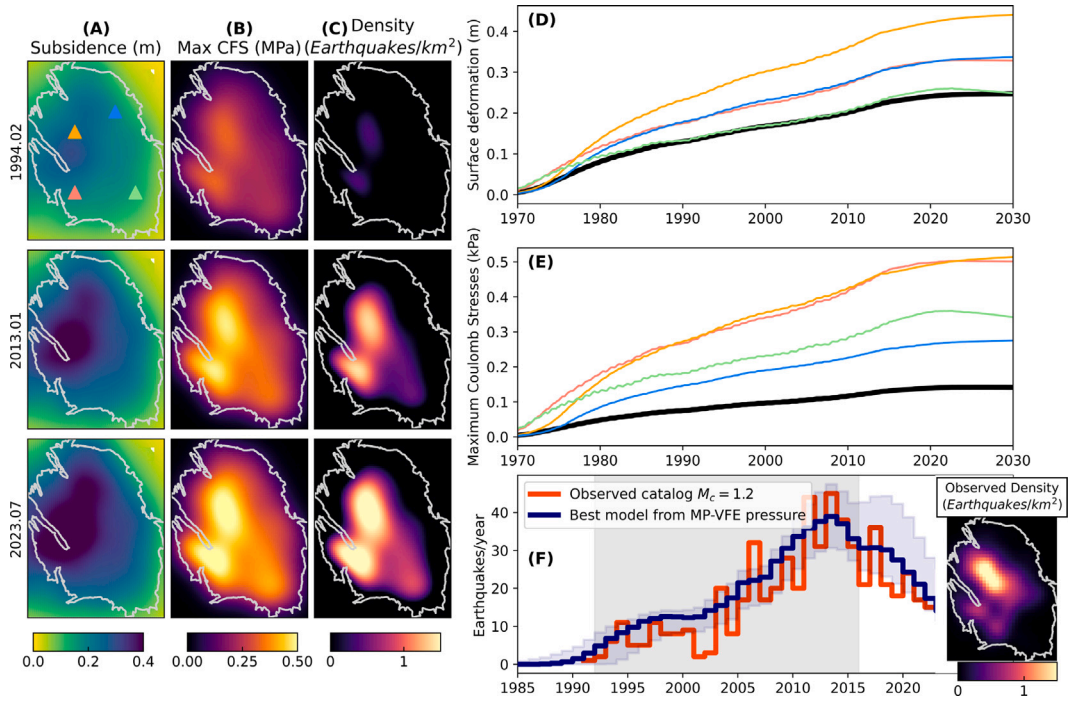

Fig. 8. Geomechanical deformation and seismicity predicted based on the best-fitting multiphase VFE model derived from history matching of the pressure measurements. (a,b,c) Map of predicted surface subsidence (a), maximum Coulomb stress changes (b), and seismicity (c) in 1994, 2013 and 2021. (d,e): Temporal evolution of the subsidence, maximum Coulomb stress change (CFS) averaged over the reservoir (black curve) and at selected locations (colored curves) corresponding to the colored triangles in panel (a). In panel (f), we show the spatial sum of earthquake density over time. The blue shaded area corresponds to the epistemic uncertainty in the seismicity rate prediction due to the uncertainties on the seismicity model parameters (see Kaveh et al. (2023)) for details. Gray shaded area represents the training period for the MCMC algorithm. The inset map in panel f represents the observed earthquake density in 2023.01 (to be compared with the bottom panel of c.).

are shown in Fig. 12 where pressure temporal variations respond almost immediately to changes in injection rates.

Significant microseismicity was recorded and relocated at Decatur after the injection began, recording more than 4000 events with magnitudes ranging from −1.5 to 1.1 (Dando et al., 2021). We show the spatio-temporal evolution of seismicity in Figs. 11 and 12. Epicenters were mainly located within a 2 km radius of the wells. Most hypocenters located the events either at the top of the Precambrian basement or in the Argenta formation (undistinguishable with the depth resolution), or on the lower end of the Mt. Simon sandstone reservoir (Fig. 11, Dando et al. (2021) and Dichiarante et al. (2021)). The temporal evolution of total and declustered (Wang and Avouac, 2025) seismicity respectively is shown in Fig. 12b in terms of cumulative earthquake numbers (black and white full lines respectively) and earthquake magnitudes (colored and white circles respectively). We observe that the declustered seismicity increases at relatively constant rate with a total number inferior to 700 events by the end of the CCS1 injection. On the contrary, the total seismicity occurs mostly through bursts of clustered seismicity occurring preferentially at the beginning of the injection (in 2011 and 2012). It reaches ~4000 events by the end of the CCS1 injection in 2015.

4.2. Pressure diffusion model

For this case, we initialize the model based on the pressure measurements based on data from the injection and monitoring (respectively CCS1 and VW1) wells (Greenberg, 2021, https://co2datashare.org/dataset/illinois-basin-decatur-project-dataset, 2025; Silva et al., 2024; Mehnert et al., 2019). Here, following Mehnert et al. (2019) and Luu et al. (2022), we initialize residual brine saturation as constant and homogeneous with values of 0.65 and residual gas saturation to 0.01. At this time, no data is available on the temporal evolution of the position and shape of the CO_2 plume. Our ability to calibrate parameters controlling its dynamics (changes in capillary pressure, relative permeability and end-point saturations) is therefore limited.

We apply constant pressure Dirichlet boundary conditions on all boundaries of the simulated domain which is 8 km * 8 km in the horizontal plane to simulate the basin being much larger than the computational domain. Here, two main unknown model parameters spatially homogeneous and stationary in time are inverted for: the reservoir's permeability (k), and porosity (ϕ). For simplicity, we manually minimize the difference between the simulated pressure fields and the pressure measurements at CCS1 and VW1.

4.3. CO_2 plume and pressure dynamics

Our simulations of multiphase flow for the Decatur phase 1 injection are shown in Fig. 13. As expected, the CO_2 plume migrates outward from the well into the reservoir over time (Fig. 13a,c,d,e). At the end of the CCS1 injection, we predict that the plume reaches a radius of ~100 m at the lower Mt. Simon reservoir's mid-depth. In contrast, the vertically averaged over-pressure field for an isobar of 0.5 MPa reaches a radius of 3500 m away from the injection well (Fig. 13b,c,d–g).

At the end of the Decatur phase 1 injection (end of 2014), the epicenters of both the clustered and declustered seismicity reach distances >1500 m away from the CCS1 well, and their hypocenters are predominantly located in the bottom of the reservoir and inside the basement. This points toward the seismicity not being triggered by the presence of CO_2 but by the overpressure field.

The model allows (i) simulating the plume position at every point in space and time, and (ii) incorporating heterogeneous reservoir properties. When a dataset regarding the dynamics of the CO_2 plume becomes available, we will be able to incorporate calibrations of capillary pressure, relative permeability and end-point saturations into the history matching procedure. Given such calibrations, this model could be used as an efficient screening tool to evaluate whether the plume will reach potential existing reservoir faults that can lead to leakage from the

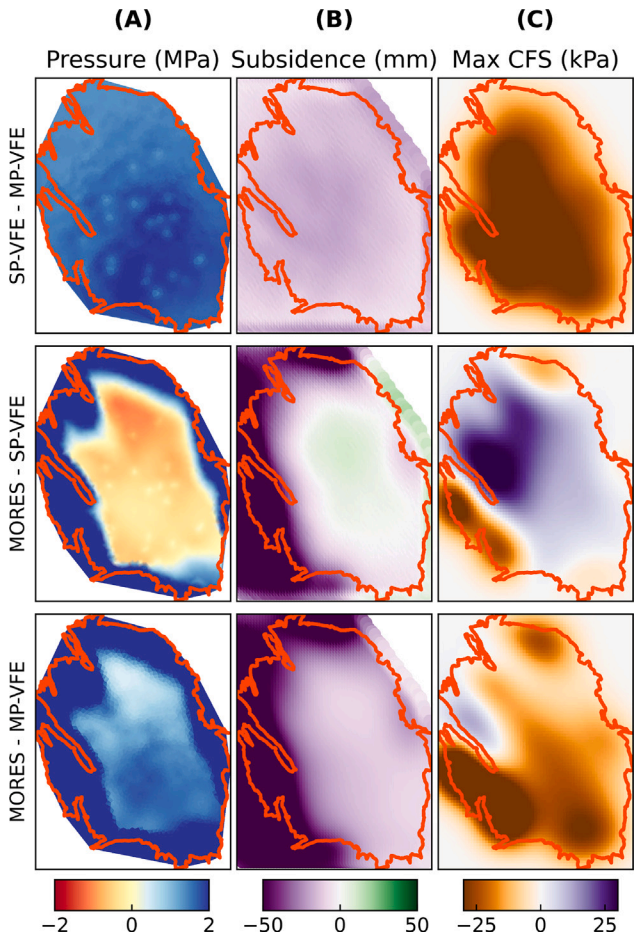

Fig. 9. Comparison of pressure (a) surface subsidence, (b) and (c) maximum Coulomb stress changes calculated with the single phase VFE model (Meyer et al., 2022), the multiphase VFE model presented in this study and the MORES model (van Oeveren et al., 2017). Comparisons are made in 2014 at the time of the maximum seismicity rate.

reservoir (Picard et al., 2011). While other modeling workflows are also very adapted for this task (Nordbotten et al., 2005; Cardoso et al., 2009; Gasda, 2010; Nordbotten and Celia, 2012; Guo et al., 2014; Court et al., 2012; Cowton et al., 2018; Bandilla et al., 2019; Jenkins et al., 2019; Meyer et al., 2022), the seamless integration of the MP-VFE model into the FLOW2QUAKE framework additionally allows efficient simulations of geomechanical deformation (which the Bjørnarå et al. (2016) model can also efficiently perform) and of seismicity for the first time at this level of numerical efficiency and with traceable uncertainties (Kaveh et al., 2023).

4.4. Geomechanical deformation

We use the computed pressure field in the previous section (Fig. 13) to feed the geomechanical model (Section 2.2). The temporal evolution of maximum Coulomb stress changes (Max CFS) computed at various constant depths is shown in Fig. 14a. Cross-sections of the Max CFS field are presented in Fig. 14c-f at different times. Its values are maximum inside the reservoir (~0.2–0.3 MPa) due to pore pressure increases which destabilize optimally oriented faults that would be present inside the reservoir (Fig. 14a, orange curve). CFS changes in the basement are due to poroelastic stress changes in our configuration and decrease with distance to the basement top from ~0.04 MPa at 1 m to ~0.006 MPa at 100 m below the reservoir (Fig. 14a, yellow to purple curves).

Several methods exist for modeling CO2 storage with geomechanical deformation, each with varying levels of complexity and computational cost. Fully 3D coupled models (Rutqvist, 2011, 2012; Vilarrasa et al., 2010; Celia et al., 2015; Jha and Juanes, 2014), offer the highest accuracy by solving the coupled flow and geomechanics equations simultaneously across the entire 3D domain, but are computationally expensive. Vertically integrated models, like those by Andersen et al. (2017) and Bjørnarå et al. (2016), present a balance between accuracy and efficiency by integrating the governing equations vertically. This simplifies the problem while still capturing key coupled processes. Sequential coupling (this work, or Silva et al. (2024)) simplifies the process further by solving flow and geomechanics separately, but can sacrifice accuracy as the full interactions between flow and deformation might not be captured. It has been shown (Smith et al., 2022) that this approach captures well the physics of the coupled flow and geomechanics in porous, thin reservoirs. It remains however an important exercise left for further work that of comparing the computational efficiency and accuracy of vertically integrated models for flow and geomechanics using (1) fully coupled hydro-geomechanical coupling (Bjørnarå et al., 2016), (2) pre-computed mechanical response functions (Andersen et al., 2017), (3) or sequentially coupled models (this work).

4.5. Seismicity

Because most of the declustered seismicity nucleates right below the basement top (Fig. 11b), we use the stress field computed at 1 m below the basement's top (Fig. 14a, yellow curve) to feed our seismicity model (Fig. 14b). The temporal evolution of forecasted seismicity rates (blue curves) is remarkably consistent toward the observed earthquake numbers (orange curve). When we compute the 95% confidence intervals (CI) on the number of earthquakes (green shaded curves, Kaveh et al. (2023)), most of the earthquakes are captured by the uncertainty on our simulations. It is remarkable that, given he simplicity (few calibration parameters and high computational efficiency) of our modeling workflow, we can capture most of the seismicity temporal variations. When comparing the spatial earthquake density (Fig. 14c), we notice that the magnitude of earthquake densities are similar in modeled and observed seismicity. However, the spatial distribution of earthquakes has larger discrepancies in terms of the affected area. This is reasonable given the simplicity of our model (axisymmetric diffusion and mechanical properties). Without prior information about the faults which can be preferential channels for fluid flow and preferential sites for earthquake nucleation, it would not be possible to improve the spatial match of seismicity.

Other modeling approaches have been used to study and forecast seismicity in the Decatur phase 1 project. Recently, Silva et al. (2024) developed a one-way coupled flow and geomechanical model to analyze the slip tendency in pre-existing faults (inferred from geophysical and seismicity data) in a full 3D model. They demonstrated that the lack of temporal correlation between the total seismicity (non-declustered) and the injected volume or pressure must have been in its majority due to fluid flow along faults that cross-cut through the reservoir and basement, connecting these units hydraulically. While this approach brings important insights for the seismicity generation mechanism, it loses forecasting power due to (1) the high computational expense of the 3D modeling, and (2) the need to pre-define the faults' geometries and orientations that will be subject to fluid and stress perturbations during CCS operations (Williams-Stroud, 2022; Greenberg, 2021; Silva et al., 2024).

A recent study that successfully applied Rate and State theory to forecast declustered seismicity (albeit using simpler methods for declustering the seismicity catalogue) is that of Luu et al. (2022). There, the authors used fully coupled 3D flow and geomechanical models which fed stress changes to the original Dieterich (1994) seismicity generation model. That study clearly established that the physics of poroelastic stress changes cannot account for the clustered seismicity because neither the physics of aftershocks, nor of fluid diffusion along faults

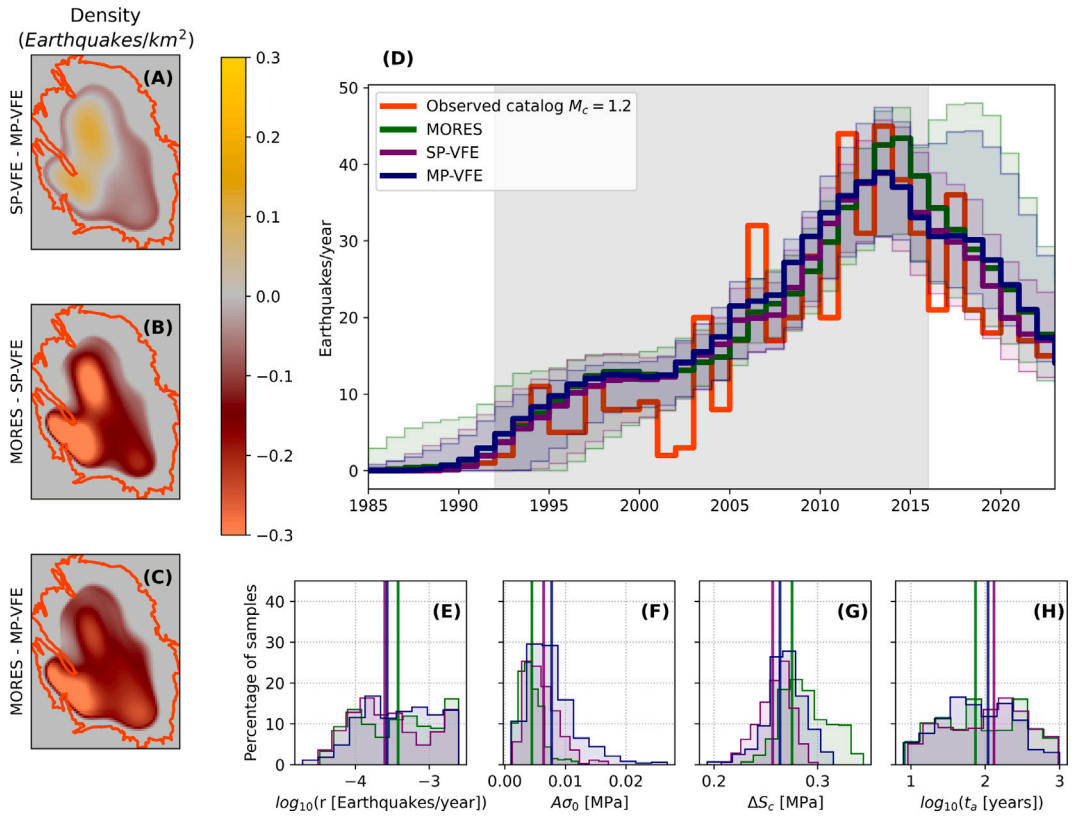

Fig. 10. Model comparison of seismicity computed using yearly data (see Acosta et al. (2023) and Section 2.2 for details). (a, b, c) Show the differences of seismicity density predicted by the Threshold Rate and State model (Heimisson et al., 2022) until 2020 for (a) single phase VFE model from Meyer et al. (2022) to current multiphase VFE model; (b) single phase VFE to MORES model (van Oeveren et al., 2017) ; and (c) current multiphase VFE model to MORES model. Panel (d) shows the comparison of the temporal evolution of seismicity rates including epistemic uncertainty (Kaveh et al., 2023) for the three models presented here. Orange shows the observed seismicity rates using $M_c = 1.2$. Gray shaded area shows the training period for all the models. Panels (e, f, g, h) show the distributions of TRS model parameters (r, $A\sigma_0$, CFS_c, and t_a) from the MCMC inversion method in percentage of samples for each parameter respectively. The best fitting models appear as vertical lines.

crosscutting the reservoir and the basement are included in these models. We can highlight several advantages of our modeling approach with respect to Luu et al. (2022) while both predictions for the declustered seismicity are comparable: (1) the number of calibration parameters is reduced from 100^+ to 5 in our model. (2) Their approach needs to impose an initial stress state in the different layers of the 3D "cake" model while here we do not need to impose an initial stress state (Smith et al., 2022). (3) Due to the simplicity of our model, it is straightforward to incorporate and propagate uncertainties in the seismicity generation process (both epistemic due to parameter estimation and aleatoric due to seismicity nucleating as a non-homogeneous Poisson process driven by the simulated rates Kaveh et al., 2023). To the best of our knowledge this work is the first study that allows explaining real seismicity for the Decatur CCS project while keeping very high computational efficiency and traceable uncertainties.

5. Application to carbon capture and storage in the Quest CCS project

In this section, we use the VFE model to study CO_2 storage in a sloping reservoir. The objective is to demonstrate how the integrated model can be useful in basins where several projects are being developed, each with its own leased area. We simulate scenarios based on publicly available information regarding the Quest industrial scale CCS project in Alberta (Canada). The project started in 2015 and has injected over 6×10^9 kg of CO_2 up until January, 2022 (Shell, 2022). We implemented the VFE reservoir model using the geometry shown in Fig. 15 and combined it with the workflow for geomechanical modeling (Section 2.2). Because the dataset available is less complete than the Groningen case study, we present only relatively simple scenarios which are designed to show the model's readiness to integrate data for the injection problem.

5.1. The Quest CCS site

The Quest carbon capture facility aims at capturing ~35% of the emitted CO_2 from a bitumen upgrading facility in Alberta, CA (Shell, 2010). The captured CO_2 is dried and compressed into a liquid. It is then transported through a 60 km underground pipeline to a storage site in Fort Saskatchewan (Fig. 15a, Shell (2010)). The Basal Cambrian Sands (BCS) formation was chosen to serve as a permanent storage site as it is overlain by a thick layer of impermeable shale which prevents upward CO_2 leakage. The BCS is a porous (~17%) and permeable ($\sim 1000 \times 10^{-15}$ m^2) sandstone rock formation. The leased area of interest (red contour in Fig. 15) at the Quest CCS site is approximately 50 km by 50 km in horizontal dimension, has a thickness of approximately 45 m and presents a slope of ~1% from South-West to North-East (Fig. 15b).

The supercritical CO_2 is injected into the Basal Cambrian Sands at a depth of ~2.2 km below the ground through three main injection wells (spaced apart by ~6 km) at a pressure of ~10 MPa. An average of 1.2 Mt (1.2×10^9 kg) CO_2 are injected into the BCS formation each year. The CO_2 plume is monitored using a network of observation wells, and a geophysical monitoring system (Harvey et al., 2022). As of December 2021, the Quest CCS project had injected 6.8 million tonnes of CO_2 into the Basal Cambrian Sandstone without any reported leak (Shell, 2022). The CO_2 plume migrates through the Basal Cambrian Sandstone in a north-westerly direction. The migration rate of the plume is approximately 100 m per year (Shell, 2022). An *a-priori* assessment of the expected CO_2 plume footprint, the associated reservoir deformation

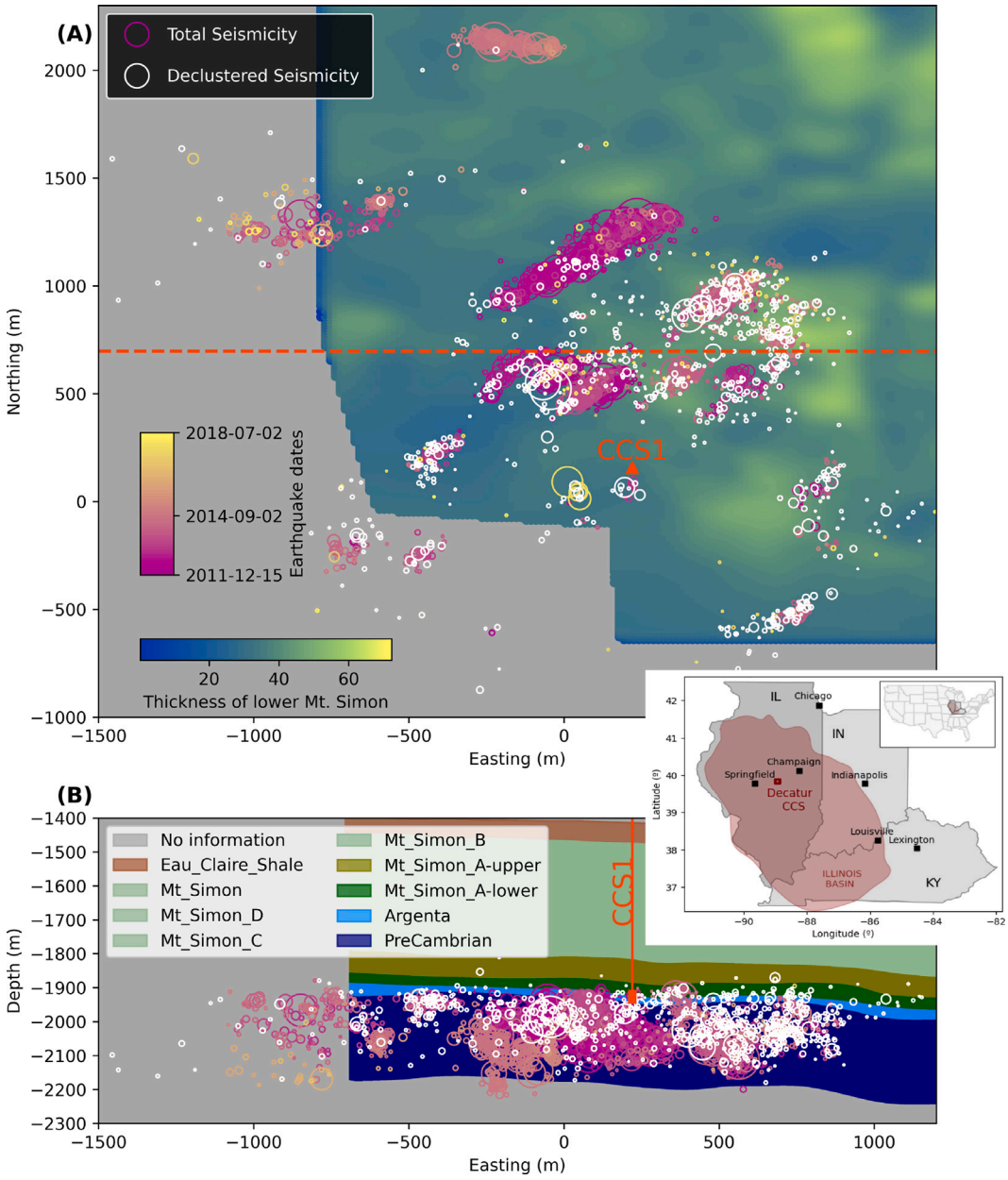

Fig. 11. The Decatur phase 1 site and associated seismicity (inset shows a location map in the Illinois basin). a. Map of the Decatur CCS site. Background color represents the thickness of the injection formation (lower Mt. Simon https://co2datashare.org/dataset/illinois-basin-decatur-project-dataset, 2025). Seismicity is represented by open circles (color-coded by date shows the total seismicity (Dando et al., 2021) and white shows the declustered seismicity (Wang and Avouac, 2025)). Sizes encode magnitudes as shown in Fig. 12b. The position of the injection well is shown in orange. b. Easting-Depth cross-section of the subsurface near the injection location. Different geologic layers are shown in color. Seismicity and well position are shown as in panel a.

and induced seismicity can be fundamental to ensure the long-term safety and sustainability of the project. Note that the Alberta basin is expected to host several projects like QUEST which could interact with one another. The current modeling workflow would be a useful tool to assess the collective and relative impact of the various operations on the pressure field, geomechanical deformation and seismicity.

5.2. Diffusion scenarios for the Quest CCS site

The simulation considers a flow rate of $\dot{M}$ = 1.2 Mt/year and a CO_2 temperature of T = 60 °C. Fluid thermophysical parameters are generated from the temperature values using the Coolprop library as described in Section 2.1.1. Concerning porosity (ϕ), permeability (k), we generate several scenarios with different values. Due to the high compressibility of fluids (gas and water) with respect to the solid compressibility, we can assume that they have no influence on pressure diffusion. Initially no gas is present in the reservoir. Fig. 16a, c, e, g shows map views of vertically averaged fluid pressure in the reservoir, first assuming that the top of the reservoir is perfectly planar and horizontal, for different values of porosity and permeability after 5 years of injection. These simulations show the impact of both parameters on pressure diffusion. The lower the permeability and porosity, the greater the pressure build-up in regions close to the wells. History matching using reservoir pressure measurements and information on CO_2 plume migration would help determining the values of permeability, porosity and capillary pressure model parameters with a very good accuracy albeit with a higher cost for the history matching than in the Groningen case. The reservoir geometry could also easily be modified to match any available information.

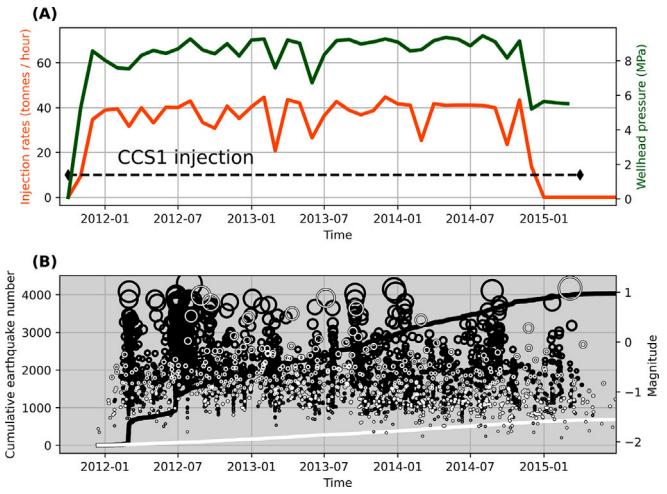

Fig. 12. Temporal evolution of a. fluid injection rate (orange), and wellhead fluid pressure (MPa) (https://co2datashare.org/dataset/illinois-basin-decatur-project-dataset, 2025); and b. Seismicity (Dando et al., 2021). The total seismicity is shown as empty black circles, declustered seismicity is shown in white. Circle sizes represent magnitude on the right y-axis. Cumulative earthquake number is shown in the left y-axis, black for total seismicity and white for declustered seismicity.

In complement, we illustrate the effect of reservoir topography on pressure diffusion using the system of Eqs. B10 & B11 (Fig. 16b, d, f, h). The top of the reservoir dips toward the southwest by about 4° (Fig. 15). This slope could affect the plume geometry and pressure field. A comparison of the two models with and without the effect of the reservoir slope is shown in Fig. 17. In such a sloping reservoir, with the parameters used in our simulation, the effect of the reservoir topography needs to be accounted for to ensure the accuracy of the simulations and potential interactions between the different projects hosted in the same formation (Gasda, 2010; Afanasyev et al., 2022).

For the same diffusion scenarios as in Fig. 16a–d, we present the gas column height in Fig. 17. We observe that given the slope of the Quest reservoir formation, and the duration of our simulations (5 years pressure equilibrium, 25 years injection, and 25 years wait), the shape of the gas plume can be heavily affected by the sloping topography for the cases of high permeability (Fig. 17a). The well-to-well interaction in terms of pressure field does generate slight asymmetry in the plume contours (Fig. 17). We highlight that even in extreme scenarios, the CO_2 would remain inside the area of interest where the leased permit is attributed to the operating company (Fig. 17a). This model could be calibrated 4D time-lapse subsurface tomography to track the plume shape over time and do the history matching procedure on those datasets (Chadwick et al., 2010; Cowton et al., 2018)

5.3. Geomechanical deformation scenarios for the Quest CCS site

We compute different scenarios of geomechanical deformation with and without topography effects. Fig. 18, shows that the slope of the reservoir does not have a significant impact on the amplitude and pattern of surface uplift. Interestingly, during the lifetime of the project, the predicted uplift signal remains too small to be measurable with SAR interferometry (<5 mm). For reference, we use an uniaxial compressibility of 1×10^{-10} Pa^{-1} but this value could be inverted from surface deformation measurements. Although the surface deformation might be too small to calibrate the compressibility of the reservoir using geodetic or SAR interferometry measurements as done in Smith et al. (2019) and Li et al. (2024), we expect that enhanced datasets from borehole strain or distributed strain sensing could provide a useful tool to that end.

Overall, we show in this section that the model is ready for data assimilation. Our fully integrated simulation of pressure diffusion, geomechanical deformation (and potential seismicity) can be fed data and calibrated against observations when they become available.

5.4. Comparison of multiphase and single phase VFE models for CO_2 injection scenarios

In this section we compare the results coming from a SP-VFE model and our MP-VFE model for the case of CO_2 injection in the geometry of Quest. Naturally, the SP-VFE model does not provide any information on the position of the CO_2 plume. Regarding the pressure field, from Section 3.5, we observed that for the case of gas extraction, the impact of using MP-VFE versus SP-VFE in the geomechanical deformation can be important but its effect on the seismicity generation process can be marginal depending on the reservoir geometry and operation history. It could in theory be argued that single phase flow models would suffice to capture the pressure field in CO_2 injection processes if the main objective is to forecast seismicity.

To this end, we test how affected the pressure field would be if the SP-VFE model (Meyer et al., 2022) was used (Fig. 19). Since we do not have any information on the gas column height that should be used for this model, we test three values of the initial gas column height ratio (0.5%, 1%, and 1.5%) and compare with the results of the MP-VFE model of Fig. 19 ($k = 1 \times 10^{-13}$ m^2, $\phi = 0.3$). We observe that the imposed gas column height ratio has a drastic control on the pressure field and can lead to differences larger than 4 MPa toward the MP-VFE results in the parameter space tested. The case with gas column height ratio of 1.5% reasonably matches the simulation results at the observation time. It is noteworthy that the value is chosen to match the prediction of the MP-VFE model and cannot (to the best of our knowledge) be estimated independently. A clear benefit of the MP-VFE model is that this quantity is solved for.

6. Conclusions

This paper presents the integration of a two-phase flow model developed using the Vertical Flow Equilibrium assumption (Section 2.1.1) into a workflow to simulate geomechanical deformation and induced seismicity (Section 2.2). The VFE assumption allows for a significant reduction of the computational cost compared to classical 3D simulations while maintaining high accuracy. We demonstrated its ability for calculations of subsurface deformation and induced seismicity in real case studies.

The model was applied to gas extraction **in Groningen gas field** (Section 3), there the model:

- shows remarkable performance compared to the operator's flow model and to a previously existing single phase VFE model.
- improves the history match to pressure data by ≈38% with respect to SP-VFE while having only 3 free parameters.
- allows computing the height of the gas column during the extraction history at reduced computational cost.
- presents an improved error toward seismicity data with respect to the output from the MORES and SP-VFE models.

The model was also applied to **simulate CO_2 injection in the Decatur phase 1** (Section 4) project where data has recently become available (https://co2datashare.org/dataset/illinois-basin-decatur-project-dataset, 2025). There, our modeling workflow integrating the MP-VFE model:

- allows forecasting the spatio-temporal evolution of the pressure field and plume due to CO_2 injection.
- provides a remarkably good match to the temporal evolution of seismicity caused by fluid injection (overpressure and stress transfer).

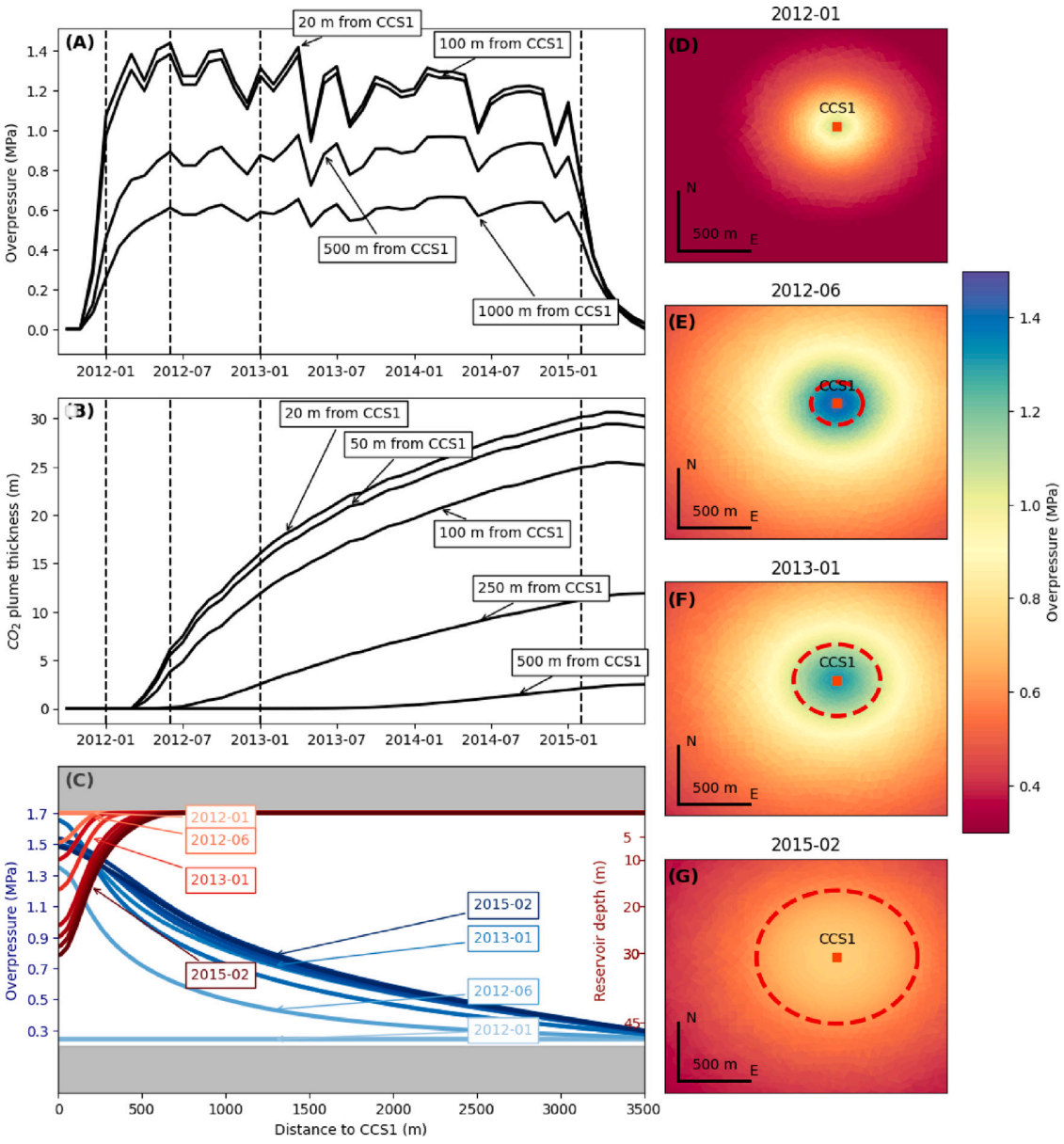

Fig. 13. Simulated CO_2 plume and reservoir overpressure in Decatur. a. Overpressure evolution in time at different distances from the CCS1 injection well. b. Same plot as a. but for CO_2 plume thickness. Note the distances from the well sampled are much lower in b. than in a. Panel c. Plume thickness (red shades, right y-axis evolving in time toward darker colors) and fluid overpressure (blue shades, right y-axis evolving in time toward darker colors) viewed inside the reservoir bounded by gray areas. d., e., f., g. show the pressure field and plume position (1 m below the reservoir top) at different times from our simulations.

- does not allow yet explaining the seismicity not-attributed to the fluid injection (earthquake–earthquake interactions, fluid diffusion along faults, aseismic slip).

Finally, the model was applied to **simulate scenarios for CO_2 injection in the Quest CCS project** (Section 5. There, due to the lack of available data for calibration, we considered plausible scenarios for hydraulic transport properties and rock compressibility. In this case, the model:

- is ready to assimilate data and forecast fluid pressures, geomechanical deformation and potential induced seismicity.
- shows that sloping topographies considerably affect CO_2 plume migration patterns but not geomechanical deformation or seismicity .

Based on the cases presented in this paper, the modeling workflow is suitable to simulate real case examples of subsurface operations where two-phase flow physics would be required while remaining very efficient numerically. It is therefore a potential useful tool to help design operations, measurement monitoring and verification plans (Plasynski et al., 2011; Sun et al., 2021), mitigation procedures (Dempsey et al., 2014; Cheng et al., 2023) or for real-time probabilistic hazard assessment (Bourne et al., 2014; Baisch et al., 2019; Schultz et al., 2021). It would also guide operations using control and optimization methods (Gutiérrez-Oribio et al., 2023) so as to optimize operational objectives while minimizing hazard. The simulations shown here could be further improved however. For example, in the case of the Groningen gas field, our boundary conditions do not allow penetration into the depleted reservoir of the aquifers bounding it laterally (van Oeveren et al., 2017). Accounting for this effect, which is taken into account in the MORES simulations (van Oeveren et al., 2017), could further reduce

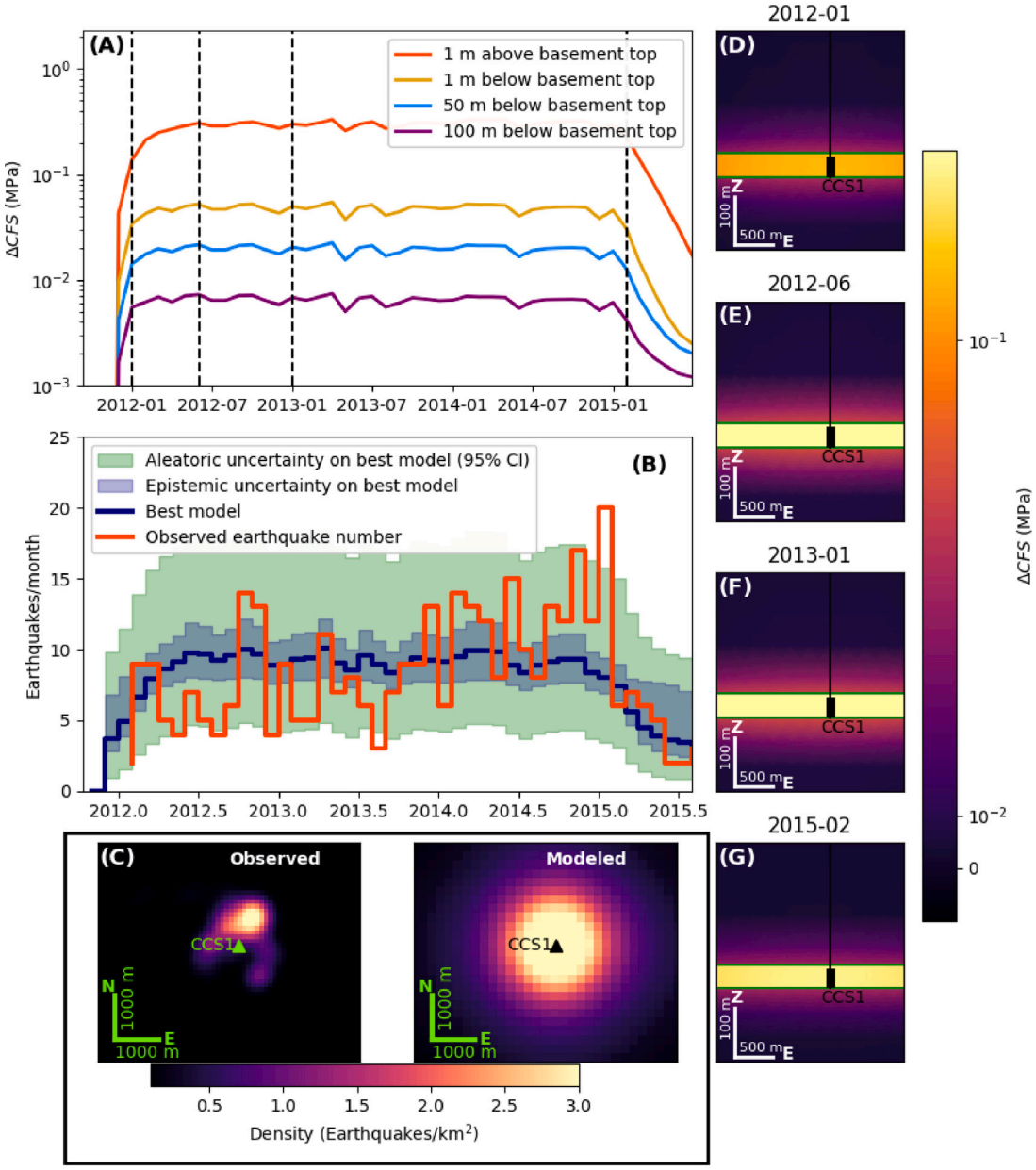

Fig. 14. Geomechanical deformation and seismicity simulations in Decatur. a. Temporal evolution of poroelastic Coulomb stress changes computed on the precambrian basement (at several depths below the reservoir-basement contact) b. Temporal evolution of monthly seismicity rates due to poroelastic stress changes. Red represents the observed declustered seismicity rates (Wang and Avouac, 2025) and blue the simulated seismicity rates. Blue shades show the epistemic uncertainty associated to the estimation of the seismicity model parameters. Green shades represent the aleatoric uncertainty associated to seismicity simulated as a non-homogeneous Poisson process driven by the rate of the best model (Kaveh et al., 2023). c. shows the spatial (East-North) seismicity density for both observed and modeled declustered seismicity computed below the reservoir at the end of CCS1 injection. d., e., f., g. East-Depth cross-sections of the Coulomb stress changes. The Lower Mt. Simon reservoir is shown bounded by green lines. Colorscale is a symmetrical logarithm allowing zero values to appear.

the pressure differences. In the case of CO_2 storage, we have ignored that CO_2 would dissolve into the brine as well as fluid–rock geochemical interactions (Abidoye et al., 2015; Zhao et al., 2024). Fluid–rock geochemical interactions are also an potentially important factor to take into account in the case of geothermal reservoirs. Finally, we have ignored thermal effects, and the possibility of phase transformations, which could also be significant in the case of CO_2 storage or geothermal operations (Vilarrasa and Rutqvist, 2017; Han et al., 2010). Indeed, supercritical CO_2 injected into the reservoir is often at temperatures much lower than the reservoir ambient one. Temperature changes may have an important impact on parameters like density and viscosity, and then on the pressure diffusion process. At this time, no data is available on the temporal evolution of the position and shape of the CO_2 plume, limiting our ability to calibrate important parameters as changes in capillary pressure, relative permeability and end-point saturations. This is an important task to perform in future studies. In the case of injection into a depleted reservoir, the ambient pressure might be too small for the CO_2 to remain supercritical. Transformation to gaseous CO_2 would lead to large temperature and pressure changes. As it stands, our VFE model does not account for such effects. Some of these effects could be included in our framework. For example, dissolution of CO_2 into the brine adds a simple sink term in the mass balance equation and this effect has already been included in VFE models (Zhao et al., 2024). Such improvements would increase the computational cost and

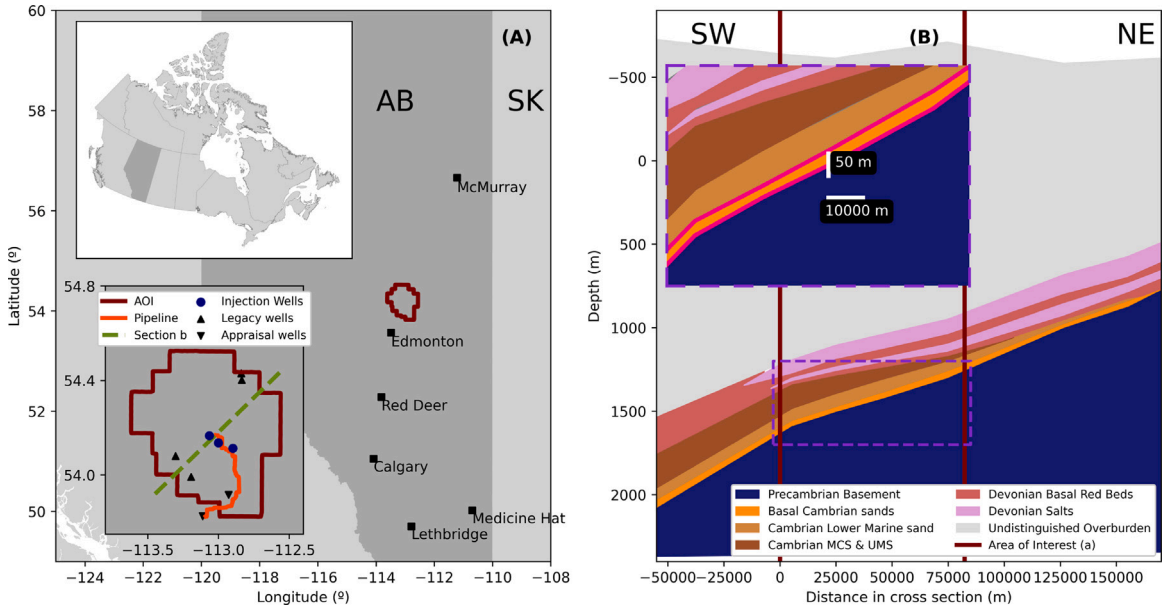

Fig. 15. The Quest CCS site. a. Map of the Quest CCS site in the Alberta basin. The map shows the lease area for the project, the pipeline for CO_2 transport and the wells (injection, existing and appraisal). A depth cross section along the green line is shown in b. The inset shows a zoom in to the area of interest limits.
Source: Modified from Shell (2010).

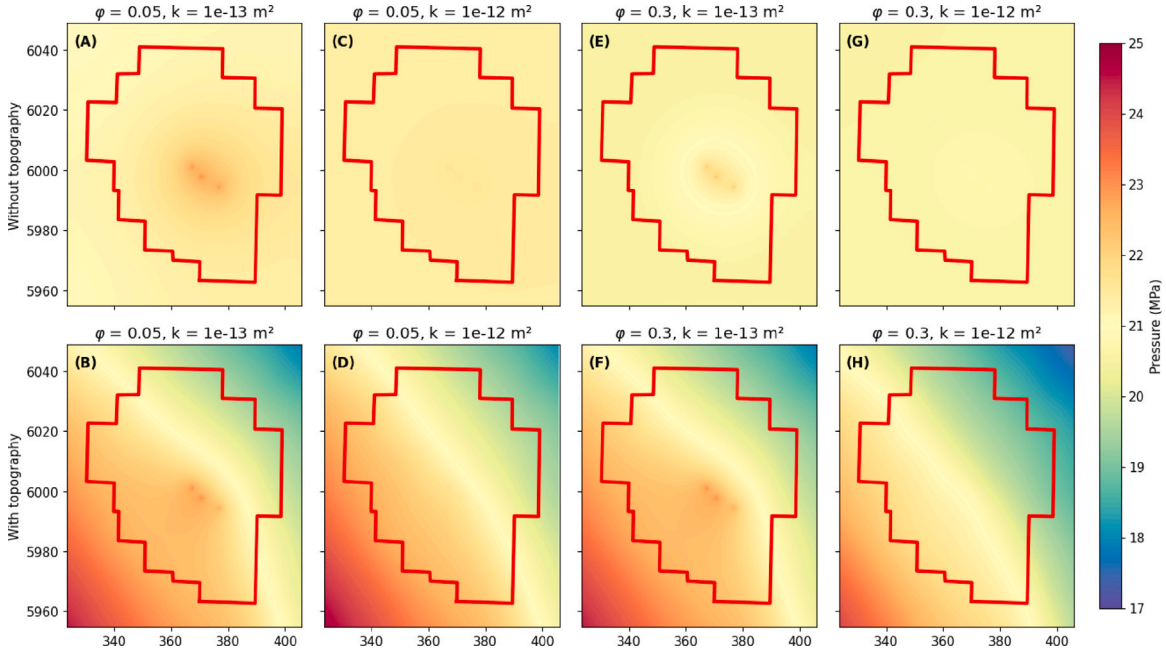

Fig. 16. Topography effects on pressure diffusion, at year 5 of gas injection (year 10 of simulation). This figure shows the effect of reservoir topography and transport properties on pressure diffusion, applied here in the case of the QUEST CCS project. Topography strongly affects pressure distribution at equilibrium, and modifies pressure values by a significant amount during reservoir operations.

imply additional free parameters that would need calibrations. The trade off between broadening the physics included in the framework and maintaining a good computational performance would therefore need to be carefully evaluated in view of the operations considered and observations available.

7. Open research

Codes necessary for the reproduction of figures in this article are available through Ledevin et al. (2024).

CRediT authorship contribution statement

Mateo Acosta: Writing – review & editing, Writing – original draft, Visualization, Validation, Supervision, Software, Project administration, Methodology, Investigation, Formal analysis, Data curation, Conceptualization. **Thomas Ledevin:** Writing – review & editing, Visualization, Validation, Software, Methodology, Investigation, Formal analysis, Data curation, Conceptualization. **Guillaume Salha:** Writing – review & editing, Validation, Software, Investigation, Formal analysis, Data curation, Conceptualization. **Charles Forestier:** Writing – review & editing, Visualization, Validation, Software, Investigation, Formal analysis, Data curation, Conceptualization. **Lucie Michelin:**

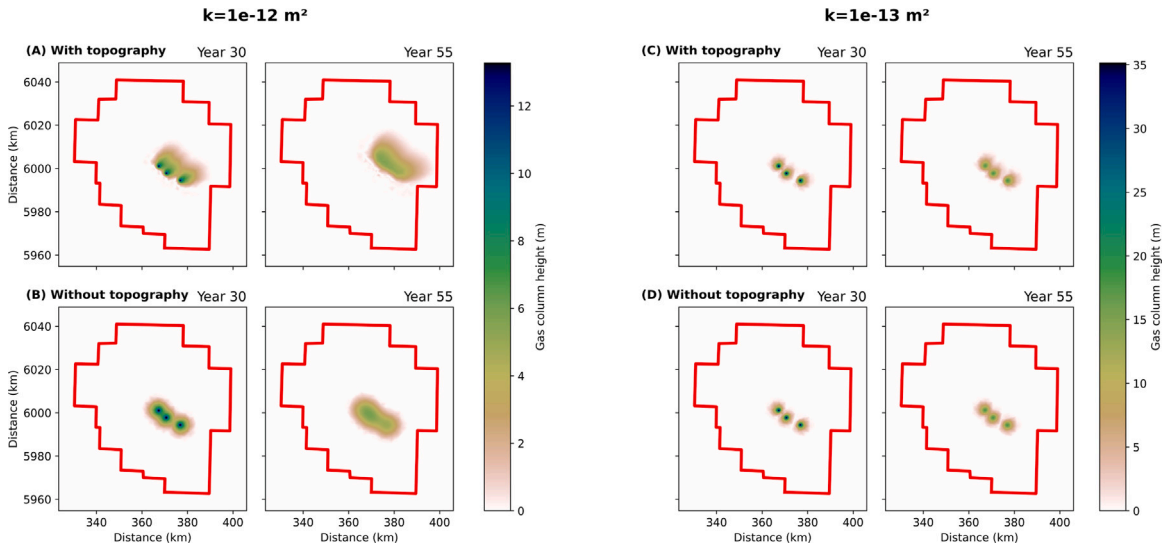

Fig. 17. Reservoir topography effects on the position and shape of the gas plume. Thickness of the gas column in plane view at different times (30 years after start of the simulation, e.g. end of the injection, and 55 years after the start of the simulation, e.g. 25 years after the end of injection). Panels a and b show the case for $k = 1 \times 10^{-12}$ m^2, with and without account for reservoir topography respectively. Panels c and d show the same but for $k = 1 \times 10^{-13}$ m^2 The plume migration is clearly visible in the cases with higher permeability. In the worst case scenario simulated here, the plume remains within the area of interest of the Quest project 25 years after the end of injection (Panel a, right-most plot). Here, panels a to d correspond to the same scenarios presented in Fig. 16a to d. All simulations presented here use $\phi = 0.05$.

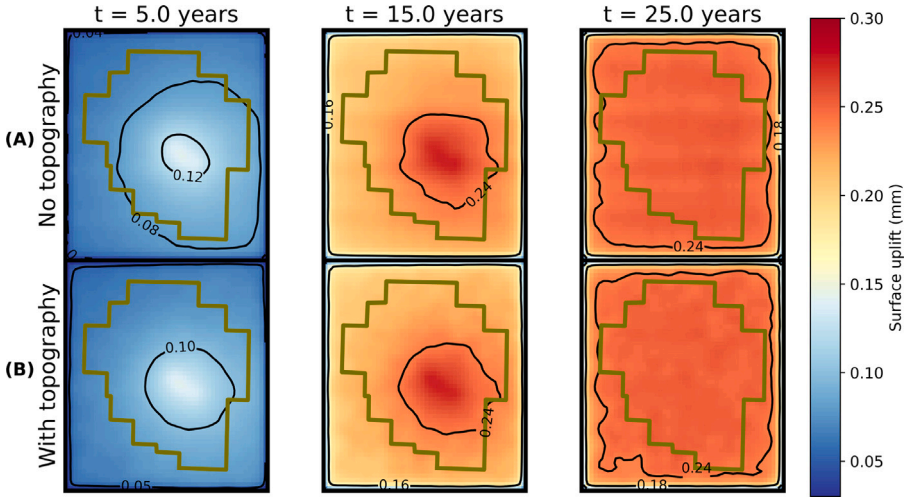

Fig. 18. Geomechanical deformation scenarios for the Quest project. We use the pressure scenario with $k = 1 \times 10^{-13}$ m^2, and $\phi = 0.3$ Panel A shows the cumulative surface uplift since the start of injections for a model not accounting for reservoir topography (either in the reservoir model or the geomechanical model) at labeled times after start of injections. Panel B shows the same as A but for models accounting for reservoir topography. The cumulative subsidence is not significantly affected by accounting or not for the reservoir geometry.

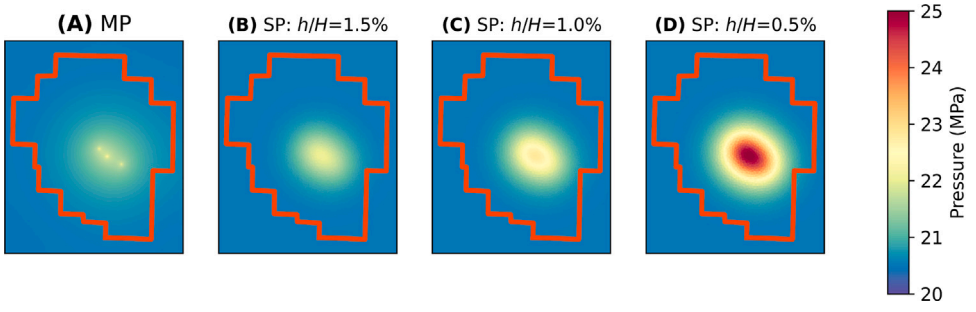

Fig. 19. Comparison of Multi phase VFE model and Single phase VFE model for the Quest reservoir for the scenario with $k = 1 \times 10^{-13}$ m^2 and $\phi = 0.3$. Panel A shows the multiphase flow pressure field at the end of the injection scenario. Panels B, C, D show the pressure field at the same time but for the single phase VFE model (Meyer et al., 2022) using initial gas column height ratios chosen arbitrarily to 1.5, 1, and 0.5% respectively.

Validation, Investigation, Formal analysis. **Xiaojing Fu:** Writing – review & editing, Supervision, Project administration, Methodology, Investigation, Funding acquisition, Formal analysis, Conceptualization. **Jean-Philippe Avouac:** Writing – review & editing, Supervision, Investigation, Formal analysis, Conceptualization.

Declaration of competing interest

The authors declare that they have no known competing financial interests or personal relationships that could have appeared to influence the work reported in this paper.

Acknowledgments

This study was supported by the NSF/IUCRC Geomechanics and Mitigation of Geohazards (National Science Foundation, USA award # 1822214). T.L. acknowledges École Polytechnique, FR for its financing support through the Chaire Energies Durables. M.A. Acknowledges funding from the Swiss National Science Foundation through grant P2ELP2195127 and from Caltech's Resnick sustainability institute, USA. We gratefully acknowledge data and support from Shell Global Solutions, USA. We gratefully acknowledge discussions with Guanli Wang and Adrian Moure. Authors declare that they have no competing interests.

Appendix A. Supplementary data

Supplementary material related to this article can be found online at https://doi.org/10.1016/j.ijggc.2025.104388.

Data availability

All data and codes can be found in: doi: 10.17605/OSF.IO/WSH32.

References

Abidoye, L.K., Khudaida, K.J., Das, D.B., 2015. Geological carbon sequestration in the context of two-phase flow in porous media: a review. Crit. Rev. Environ. Sci. Technol. 45 (11), 1105–1147.

Acosta, M., Avouac, J.-P., Smith, J.D., Sirorattanakul, K., Kaveh, H., Bourne, S.J., 2023. Earthquake nucleation characteristics revealed by seismicity response to seasonal stress variations induced by gas production at Groningen. Geophys. Res. Lett. 50 (19), e2023GL105455.

Afanasyev, A., Vedeneeva, E., Grechko, S., 2022. Scaling analysis for a 3-D CO2 plume in a sloping aquifer at a late stage of injection. J. Nat. Gas Sci. Eng. 106, 104740.

Andersen, O., Nilsen, H.M., Gasda, S.E., 2017. Vertical equilibrium flow models with fully coupled geomechanics for CO2 storage modeling, using precomputed mechanical response functions. Energy Proced. 114, 3113–3131.

Bachu, S., Bonijoly, D., Bradshaw, J., Burruss, R., Holloway, S., Christensen, N.P., Mathiassen, O.M., 2007. CO2 storage capacity estimation: Methodology and gaps. Int. J. Greenh. Gas Control. 1 (4), 430–443.

Baisch, S., Koch, C., Muntendam-Bos, A., 2019. Traffic light systems: To what extent can induced seismicity be controlled? Seismol. Res. Lett. 90 (3), 1145–1154.

Bandilla, K.W., Guo, B., Celia, M.A., 2019. A guideline for appropriate application of vertically-integrated modeling approaches for geologic carbon storage modeling. Int. J. Greenh. Gas Control..

Bell, I.H., Wronski, J., Quoilin, S., Lemort, V., 2014. Pure and Pseudo-pure Fluid Thermophysical Property Evaluation and the Open-Source Thermophysical Property Library CoolProp. Ind. Eng. Chem. Res. 53 (6), 2498–2508. http://dx.doi.org/10.1021/ie4033999, URL http://pubs.acs.org/doi/abs/10.1021/ie4033999.

Bemer, E., Boutéca, M., Vincké, O., Hoteit, N., Ozanam, O., 2001. Poromechanics: From linear to nonlinear poroelasticity and poroviscoelasticity. Oil & Gas Sci. Technol. 56 (6), 531–544.

Bjørnarå, T.I., Nordbotten, J.M., Park, J., 2016. Vertically integrated models for coupled two-phase flow and geomechanics in porous media. Water Resour. Res. 52 (2), 1398–1417.

Bourne, S., Crouch, S., Smith, M., 2014. A risk-based framework for measurement, monitoring and verification of the Quest CCS Project, Alberta, Canada. Int. J. Greenh. Gas Control. 26, 109–126.

Bourne, S., Oates, S., 2017. Extreme threshold failures within a heterogeneous elastic thin sheet and the spatial-temporal development of induced seismicity within the Groningen gas field. J. Geophys. Res.: Solid Earth 122 (12), 10–299.

Bourne, S., Oates, S., Van Elk, J., 2018. The exponential rise of induced seismicity with increasing stress levels in the Groningen gas field and its implications for controlling seismic risk. Geophys. J. Int. 213 (3), 1693–1700.

Brodsky, E.E., Lajoie, L.J., 2013. Anthropogenic seismicity rates and operational parameters at the Salton Sea Geothermal Field. Sci. 341 (6145), 543–546.

Buijze, L., van den Bogert, P.A., Wassing, B.B., Orlic, B., ten Veen, J., 2017. Fault reactivation mechanisms and dynamic rupture modelling of depletion-induced seismic events in a Rotliegend gas reservoir. Neth. J. Geosci. 96 (5), s131–s148.

Burkitov, U., van Oeveren, H., Valvatne, P., 2015. Groningen field review 2015 subsurface dynamic modelling report. NAM.

Candela, T., Osinga, S., Ampuero, J.-P., Wassing, B., Pluymaekers, M., Fokker, P.A., van Wees, J.-D., de Waal, H.A., Muntendam-Bos, A.G., 2019. Depletion-induced seismicity at the Groningen gas field: Coulomb rate-and-state models including differential compaction effect. J. Geophys. Res.: Solid Earth 124 (7), 7081–7104.

Cardoso, M.A., Durlofsky, L.J., Sarma, P., 2009. Development and application of reduced-order modeling procedures for subsurface flow simulation. Internat. J. Numer. Methods Engrg. 77 (9), 1322–1350.

Celia, M.A., Bachu, S., Nordbotten, J.M., Bandilla, K.W., 2015. Status of CO2 storage in deep saline aquifers with emphasis on modeling approaches and practical simulations. Water Resour. Res. 51 (9), 6846–6892.

Chadwick, A., Williams, G., Delepine, N., Clochard, V., Labat, K., Sturton, S., Buddensiek, M.-L., Dillen, M., Nickel, M., Lima, A.L., et al., 2010. Quantitative analysis of time-lapse seismic monitoring data at the Sleipner CO 2 storage operation. Lead. Edge 29 (2), 170–177.

Cheng, Y., Liu, W., Xu, T., Zhang, Y., Zhang, X., Xing, Y., Feng, B., Xia, Y., 2023. Seismicity induced by geological CO2 storage: A review. Earth-Sci. Rev. 239, 104369.

Court, B., Bandilla, K.W., Celia, M.A., Janzen, A., Dobossy, M., Nordbotten, J.M., 2012. Applicability of vertical-equilibrium and sharp-interface assumptions in CO2 sequestration modeling. Int. J. Greenh. Gas Control. 10, 134–147.

Coussy, O., 2004. Poromechanics. John Wiley & Sons.

Cowton, L., Neufeld, J., White, N., Bickle, M., Williams, G., White, J., Chadwick, R., 2018. Benchmarking of vertically-integrated CO2 flow simulations at the Sleipner Field, North Sea. Earth Planet. Sci. Lett. 491, 121–133.

Dahm, T., Hainzl, S., 2022. A Coulomb Stress Response Model for Time-Dependent Earthquake Forecasts. J. Geophys. Res.: Solid Earth 127 (9), e2022JB024443.

Dando, B., Goertz-Allmann, B., Kühn, D., Langet, N., Dichiarante, A., Oye, V., 2021. Relocating microseismicity from downhole monitoring of the Decatur CCS site using a modified double-difference algorithm. Geophys. J. Int. 227 (2), 1094–1122.

de Jager, J., Visser, C., 2017. Geology of the Groningen field – an overview. Neth. J. Geosci. 96 (5), s47–s54.

Dempsey, D., Kelkar, S., Pawar, R., 2014. Passive injection: A strategy for mitigating reservoir pressurization, induced seismicity and brine migration in geologic CO2 storage. Int. J. Greenh. Gas Control. 28, 96–113.

Dempsey, D., Suckale, J., 2017. Physics-based forecasting of induced seismicity at Groningen gas field, the Netherlands. Geophys. Res. Lett. 44 (15), 7773–7782.

Detournay, E., Cheng, A.H.-D., 1993. Fundamentals of poroelasticity. In: Analysis and Design Methods. Elsevier, pp. 113–171.

Dichiarante, A.M., Langet, N., Bauer, R., Goertz-Allmann, B., Williams-Stroud, S.C., Kühn, D., Oye, V., Greenberg, S., Dando, B., 2021. Identifying geological structures through microseismic cluster and burst analyses complementing active seismic interpretation. Tectonophysics 820, 229107.

Dieterich, J., 1994. A constitutive law for rate of earthquake production and its application to earthquake clustering. J. Geophys. Res.: Solid Earth 99 (B2), 2601–2618.

Gasda, S.E., 2010. Numerical Models for Evaluating CO2 Storage in Deep Saline Aquifers: Leaky Wells and Large-Scale Geological Features (Ph.D. thesis). Princeton University.

Geertsma, J., 1973. Land subsidence above compacting oil and gas reservoirs. J. Pet. Technol. 25 (06), 734–744.

Gholami, R., Raza, A., Iglauer, S., 2021. Leakage risk assessment of a CO2 storage site: A review. Earth-Sci. Rev. 223, 103849.

Goertz-Allmann, B.P., Langet, N., Iranpour, K., Kühn, D., Baird, A., Oates, S., Rowe, C., Harvey, S., Oye, V., Nakstad, H., 2024. Effective microseismic monitoring of the Quest CCS site, Alberta, Canada. Int. J. Greenh. Gas Control. 133, 104100.

Greenberg, S., 2021. An Assessment of Geologic Carbon Sequestration Options in the Illinois Basin: Phase III. Tech. Rep, Univ. of Illinois.

Grigoli, F., Cesca, S., Priolo, E., Rinaldi, A.P., Clinton, J.F., Stabile, T.A., Dost, B., Fernandez, M.G., Wiemer, S., Dahm, T., 2017. Current challenges in monitoring, discrimination, and management of induced seismicity related to underground industrial activities: A European perspective. Rev. Geophys. 55 (2), 310–340.

Guo, B., Bandilla, K.W., Doster, F., Keilegavlen, E., Celia, M.A., 2014. A vertically integrated model with vertical dynamics for CO2 storage. Water Resour. Res. 50 (8), 6269–6284.

Gutiérrez-Oribio, D., Tzortzopoulos, G., Stefanou, I., Plestan, F., 2023. Earthquake control: An emerging application for robust control. theory and experimental tests. IEEE Trans. Control Syst. Technol. 31 (4), 1747–1761.

Han, W.S., Stillman, G.A., Lu, M., Lu, C., McPherson, B.J., Park, E., 2010. Evaluation of potential nonisothermal processes and heat transport during CO2 sequestration. J. Geophys. Res.: Solid Earth 115 (B7).

Hao, Y., Sun, Y., Nitao, J., 2012. Overview of NUFT: A versatile numerical model for simulating flow and reactive transport in porous media. Groundw. React. Transp. Model. 212–239.

Harvey, S., Hopkins, J., Kuehl, H., O'Brien, S., Mateeva, A., 2022. Quest CCS facility: Time-lapse seismic campaigns. Int. J. Greenh. Gas Control. 117, 103665.

Heimisson, E.R., Smith, J.D., Avouac, J.-P., Bourne, S.J., 2022. Coulomb threshold rate-and-state model for fault reactivation: application to induced seismicity at Groningen. Geophys. J. Int. 228 (3), 2061–2072.

Illinois Basin - Decatur Project Dataset doi:10.11582/2022.00017 URL https://co2datashare.org/dataset/illinois-basin-decatur-project-dataset.

Im, K., Avouac, J.-P., 2021. On the role of thermal stress and fluid pressure in triggering seismic and aseismic faulting at the Brawley Geothermal Field, California.. Geotherm. 97, 102238.

Jenkins, L.T., Foschi, M., MacMinn, C.W., 2019. Impact of pressure dissipation on fluid injection into layered aquifers. Camb. Univ. Press.

Jha, B., Juanes, R., 2014. Coupled modeling of multiphase flow and fault poromechanics during geologic CO2 storage. Energy Procedia 63, 3313–3329.

Juanes, R., Jha, B., Hager, B., Shaw, J., Plesch, A., Astiz, L., Dieterich, J., Frohlich, C., 2016. Were the May 2012 Emilia-Romagna earthquakes induced? A coupled flow-geomechanics modeling assessment. Geophys. Res. Lett. 43 (13), 6891–6897.

Kaveh, H., Batlle, P., Acosta, M., Kulkarni, P., Bourne, S.J., Avouac, J.P., 2023. Induced Seismicity forecasting with Uncertainty Quantification: Application to Groningen Gas Field. Seismol. Res. Lett..

Kelemen, P., Benson, S.M., Pilorgé, H., Psarras, P., Wilcox, J., 2019. An overview of the status and challenges of CO2 storage in minerals and geological formations. Front. Clim. 1, 9.

Keranen, K.M., Weingarten, M., 2018. Induced seismicity. Annu. Rev. Earth Planet. Sci. 46, 149–174.

Kim, T., Avouac, J.-P., 2023. Stress-Based and Convolutional Forecasting of Injection-Induced Seismicity: Application to the Otaniemi Geothermal Reservoir Stimulation. J. Geophys. Res.: Solid Earth 128 (4), e2022JB024960.

Kopp, A., Class, H., Helmig, R., 2009. Investigations on CO2 storage capacity in saline aquifers: Part 1. Dimensional analysis of flow processes and reservoir characteristics. Int. J. Greenh. Gas Control. 3 (3), 263–276.

Kuvshinov, B.N., 2008. Elastic and piezoelectric fields due to polyhedral inclusions. Int. J. Solids Struct..

Ledevin, T., Acosta, M., Michelin, L., Fu, X., Avouac, J.-P., 2024. Dataset and code repository for for the article on multiphase vertical flow equilibrium model for simulation of geomechanical deformation and seismicity induced by reservoir operations. [data set]. OSF: Open Source Fram. Osf. Io/ Wsh32 http://dx.doi.org/10.17605/OSF.IO/WSH32.

Li, Y., Acosta, M., Sirorattanakul, K., Bourne, S., Avouac, J.-P., 2024. InSAR monitoring of elastic and inelastic deformation in compacting reservoirs due to subsurface operations. J. Geophys. Res.: Solid Earth 130 (3), e2024JB030794.

Li, B., Khoshmanesh, M., Avouac, J.-P., 2021. Surface deformation and seismicity induced by poroelastic stress at the Raft River geothermal field, Idaho, USA. Geophys. Res. Lett. 48 (18), e2021GL095108.

Logg, A., Mardal, K.-A., Wells, G., 2012. Automated Solution of Differential Equations by the Finite Element Method. Springer.

Luu, K., Schoenball, M., Oldenburg, C.M., Rutqvist, J., 2022. Coupled hydromechanical modeling of induced seismicity from CO2 injection in the Illinois Basin. J. Geophys. Res.: Solid Earth 127 (5), e2021JB023496.

Marsan, D., Lengline, O., 2008. Extending earthquakes' reach through cascading. Sci. 319 (5866), 1076–1079.

Mehnert, E., Damico, J.R., Grigsby, N.P., Monson, C.C., Patterson, C.G., Yang, F., 2019. Geologic carbon sequestration in the Illinois basin: Numerical modeling to evaluate potential impacts. Circ. No. 598.

Meyer, H., Smith, J.D., Bourne, S.J., Avouac, J.-P., 2022. An integrated framework for surface deformation modeling and induced seismicity forecasting due to reservoir operations. Geol. Soc. Lond. Spec. Publ..

Muntendam-Bos, A., 2020. Clustering characteristics of gas-extraction induced seismicity in the Groningen gas field. Geophys. J. Int. 221 (2), 879–892.

Nordbotten, J.M., Celia, M.A., 2006. An improved analytical solution for interface upconing around a well. Water Resour. Res. 42 (8).

Nordbotten, J.M., Celia, M.A., 2012. Geological Storage of CO2: Modeling Approaches for Large-Scale Simulation. Wiley.

Nordbotten, J.M., Celia, M.A., Bachu, S., 2005. Injection and storage of CO 2 in deep saline aquifers: analytical solution for CO 2 plume evolution during injection. Transp. Porous Media 58, 339–360.

Oates, S., Landman, A.J., van der Wal, O., Baehr, H., Piening, H., 2022. Geomechanical, Seismological, and Geodetic Data Pertaining to The Groningen Gas Field: a Data Package Used in The "Mmax II Workshop", on Constraining the Maximum Earthquake Magnitude in the Groningen Field (Version 1.0) [Data set]. Utrecht University, http://dx.doi.org/10.24416/UU01-RHHRPY.

van Oeveren, H., Valvatne, P., Geurtsen, L., van Elk, J., 2017. History match of the Groningen field dynamic reservoir model to subsidence data and conventional subsurface data. Neth. J. Geosci. 96 (5), s47–s54.

Picard, G., Bérard, T., Chabora, E., Marsteller, S., Greenberg, S., Finley, R.J., Rinck, U., Greenaway, R., Champagnon, C., Davard, J., 2011. Real-time monitoring of CO2 storage sites: application to Illinois Basin–Decatur Project. Energy Proced. 4, 5594–5598.

Plasynski, S.I., Litynski, J.T., McIlvried, H.G., Vikara, D.M., Srivastava, R.D., 2011. The critical role of monitoring, verification, and accounting for geologic carbon dioxide storage projects. Environ. Geosci. 18 (1), 19–34.

Post, R.A., Michels, M.A., Ampuero, J.-P., Candela, T., Fokker, P.A., van Wees, J.-D., Hofstad, R.W.v.d., Heuvel, E.R.v.d., 2021. Interevent-time distribution and aftershock frequency in non-stationary induced seismicity. Sci. Rep. 11 (1), 3540.

Richter, G., Hainzl, S., Dahm, T., Zöller, G., 2020. Stress-based, statistical modeling of the induced seismicity at the Groningen gas field, The Netherlands. Environ. Earth Sci. 79 (11), 252.

Rudnicki, J.W., 1986. Fluid mass sources and point forces in linear elastic diffusive solids. Mech. Mater. 5 (4), 383–393.

Rutqvist, J., 2011. Status of the TOUGH-FLAC simulator and recent applications related to coupled fluid flow and crustal deformations. Comput. Geosci. 37 (6), 739–750.

Rutqvist, J., 2012. The geomechanics of CO 2 storage in deep sedimentary formations. Geotech. Geol. Eng. 30, 525–551.

Schultz, R., Beroza, G.C., Ellsworth, W.L., 2021. A risk-based approach for managing hydraulic fracturing–induced seismicity. Sci. 372 (6541), 504–507.

Segall, P., Lu, S., 2015. Injection-induced seismicity: Poroelastic and earthquake nucleation effects. J. Geophys. Res.: Solid Earth 120 (7), 5082–5103.

Shell, 2010. Quest carbon and storage project, Volume1: Project description. Shell Rep. 1, 1–11, URL https://open.alberta.ca/dataset/7fc3495c-4659-4712-9ee4-8fe7e39f03b8/resource/bae2d1e1-d2e6-4e0f-a779-c05912254bdb/download/01-quest-vol-1-project-description.pdf.

Shell, 2022. Quest Carbon Capture and Storage project : annual summary report 2022. Alta. Dep. Energy 1, URL https://open.alberta.ca/dataset/356aeeda-134c-4779-971c-931573400ddf/resource/8a1b4350-9634-4e66-a983-8c16199fa2e7/download/quest-annual-summary-report-2022-alberta-department-of-energy.pdf.

Silva, J.A., Khosravi, M., Yoon, H., Fehler, M., Frailey, S., Juanes, R., 2024. Mechanisms for Microseismicity Occurrence Due to CO 2 Injection at Decatur, Illinois: A Coupled Multiphase Flow and Geomechanics Perspective. Bull. Seismol. Soc. Am. 114 (5), 2424–2445.

Sirorattanakul, K., Wilding, J.D., Acosta, M., Li, Y., Ross, Z.E., Bourne, S.J., van Elk, J., Avouac, J.-P., 2024. Bursts of fast propagating swarms of induced earthquakes at the Groningen gas field. Seismol. Res. Lett. 96 (1), 130–146.

Smith, J.D., Avouac, J.-P., White, R.S., Copley, A., Gualandi, A., Bourne, S., 2019. Reconciling the long-term relationship between reservoir pore pressure depletion and compaction in the Groningen region. J. Geophys. Res.: Solid Earth 124 (6), 6165–6178.

Smith, J.D., Heimisson, E.R., Bourne, S.J., Avouac, J.-P., 2022. Stress-based forecasting of induced seismicity with instantaneous earthquake failure functions: Applications to the Groningen gas reservoir. Earth Planet. Sci. Lett. 594, 117697.

Stephenson, M.H., Ringrose, P., Geiger, S., Bridden, M., Schofield, D., 2019. Geoscience and decarbonization: current status and future directions. Pet. Geosci. 25 (4), 501–508.

Sun, Y., Liu, J., Xue, Z., Li, Q., Fan, C., Zhang, X., 2021. A critical review of distributed fiber optic sensing for real-time monitoring geologic CO2 sequestration. J. Nat. Gas Sci. Eng. 88, 103751.

Szulczewski, M., MacMinn, C., Herzog, H., Juanes, R., 2012. Lifetime of carbon capture and storage as a climate-change mitigation technology.. Proc. Natl. Acad. Sci. 109, 5185–5189.

Tamama, Y., Acosta, M., Bourne, S.J., Avouac, J.-P., 2024. Earthquake growth inhibited at higher Coulomb stress rate at groningen. Geophysical Research Letters 51 (20), e2024GL110139.

Trampert, J., Benzi, R., Toschi, F., 2022. Implications of the statistics of seismicity recorded within the Groningen gas field. Neth. J. Geosci. 101, e9.

Vilarrasa, V., Bolster, D., Olivella, S., Carrera, J., 2010. Coupled hydromechanical modeling of CO2 sequestration in deep saline aquifers. Int. J. Greenh. Gas Control. 4 (6), 910–919.

Vilarrasa, V., Rutqvist, J., 2017. Thermal effects on geologic carbon storage. Earth-Sci. Rev. 165, 245–256.

Wang, G., Avouac, J.-P., 2025. Inferring the causal structure among injection-induced seismicity with linear intensity models. Bull. Seismol. Soc. Am. http://dx.doi.org/10.1785/0120240233.

Wang, B., Kao, H., Yu, H., Visser, R., Venables, S., 2022. Physical factors controlling the diverse seismogenic behavior of fluid injections in Western Canada. Earth Planet. Sci. Lett. 589, 117555.

Wang, R., Kümpel, H.-J., 2003. Poroelasticity: Efficient modeling of strongly coupled, slow deformation processes in a multilayered half-space. Geophys. 68 (2), 705–717.

Williams-Stroud, S., 2022. Integrating induced seismicity with fault interpretation at the decatur, IL CCS projects.

Yortsos, Y.C., 1995. A theoretical analysis of vertical flow equilibrium. Transp. Porous Media 18 (2), 107–129.

Zgonnik, V., 2020. The occurrence and geoscience of natural hydrogen: A comprehensive review. Earth-Sci. Rev. 203, 103140.

Zhai, G., Shirzaei, M., Manga, M., Chen, X., 2019. Pore-pressure diffusion, enhanced by poroelastic stresses, controls induced seismicity in Oklahoma. Proc. Natl. Acad. Sci. 116 (33), 16228–16233.

Zhao, Y.H., Shakourifar, N., Shahsavar, N., Lei, Y., Zhao, B., 2024. A holistic framework for evaluating gigaton scale geological CO2 storage applied to the alberta oil sands: Physics, policy, and economics. Int. J. Greenh. Gas Control. 134, 104129. http://dx.doi.org/10.1016/j.ijggc.2024.104129, URL https://www.sciencedirect.com/science/article/pii/S1750583624000720.

Zivar, D., Kumar, S., Foroozesh, J., 2021. Underground hydrogen storage: A comprehensive review. Int. J. Hydrog. Energy 46 (45), 23436–23462.

Further reading

Gasunie, 1988. Physical properties of natural gases. p. 31, URL https://www.worldcat.org/fr/title/physical-properties-of-natural-gases/oclc/19077954.

Lie, K.-A., 2019. An introduction to reservoir simulation using MATLAB/GNU Octave: User guide for the MATLAB Reservoir Simulation Toolbox (MRST). Cambridge University Press.

Wen, G., Hay, C., Benson, S.M., 2021. CCSNet: A deep learning modeling suite for CO2 storage. Adv. Water Resour..